ANKARA YILDIRIM BEYAZIT UNIVERSITY

GRADUATE SCHOOL OF NATURAL SCIENCES



AERODYNAMIC ANALYSIS AND OPTIMIZATION OF AIRFOIL OF AN UNMANNED AERIAL VEHICLE USING CFD

M.Sc. Thesis by

Raghad BABA

Department of Mechanical Engineering

May, 2019

ANKARA

AERODYNAMIC ANALYSIS AND OPTIMIZATION OF AIRFOIL OF AN UNMANNED AERIAL VEHICLE USING CFD

A Thesis Submitted to

The Graduate School of Natural Sciences of

Ankara Yıldırım Beyazıt University

In Partial Fulfillment of the Requirements for the Degree of Master of Science in Mechanical Engineering, Department of Mechanical Engineering

by

Raghad BABA

May, 2019

ANKARA

M.Sc. THESIS EXAMINATION RESULT FORM

We have read the thesis entitled **"AERODYNAMIC ANALYSIS AND OPTIMIZATION OF AIRFOIL OF AN UNMANNED AERIAL VEHICLE"** completed by **RAGHAD BABA** under the supervision of **PROF. DR. EROL ARCAKLIOĞLU** and we certify that in our opinion it is fully adequate, in scope and in quality, as a thesis for the degree of Master of Science.

Prof. Dr. Erol ARCAKLIOĞLU

Supervisor

Prof. Dr. Abuzer ÖZSUNAR

Jury Member

Dr. Kemal BİLEN

Jury Member

Prof. Dr. Ergün ERASLAN

Director

Graduate School of Natural Sciences

I hereby declare that, in this thesis which has been prepared in accordance with the Thesis Writing Manual of Graduate School of Natural and Applied Sciences,

- All data, information and documents are obtained in the framework of academic and ethical rules,
- All information, documents and assessments are presented in accordance with scientific ethics and morals,
- All the materials that have been utilized are fully cited and referenced,
- No change has been made on the utilized materials,
- All the works presented are original,

and in any contrary case of above statements, I accept to renounce all my legal rights.

Date: 22.05.2019 **Signature:**

Name and Surname: Raghad BABA

ACKNOWLEDGMENTS

I wish to express my sincere gratitude to my thesis supervisor, Prof. Dr. Erol ARCAKLIOĞLU for his continuous and exceptional support and encouragement throughout this process. His guidance steered me in the right direction, provided me with an endless motivation, assisted me all the time of my research and while writing this thesis.

2019, 22 May **Raghad BABA**

AERODYNAMIC ANALYSIS AND OPTIMIZATION OF AIRFOIL OF AN UNMANNED AERIAL VEHICLE USING CFD

ABSTRACT

Airfoil is a substantial part of an aircraft affecting directly and significantly on the performance and efficiency of the design for that reason the airfoil selection part of the design process is an essential step affects the success of the whole aircraft design process.

In this thesis, a selection process study of an airfoil of a small unmanned aerial vehicle has been carried out. A two-dimensional computational simulation has been carried out in order to determine the optimal airfoil profile from seven different airfoils HS520, MH114, MH45, MH60, SA7035, SA7038, and SD7090 which have been chosen upon their popularity and suitability for unmanned aerial vehicles. The simulations were performed at chord Reynolds number Re= $2.4 \cdot 10^5$ low subsonic flow speed in ANSYS Fluent using the finite volume approach. Transition Shear Stress Transport (γ-Reθ) SST is used as a turbulence model. Another study also has been performed using XFOIL to compare and verify the results of the Fluent study.

The lift coefficient, the low stalling speed, the lift to drag ratio, and some stall characteristics have been set to be the criteria which have been used to select an appropriate wing airfoil which satisfies the design requirements. The aerodynamic characteristics of lift coefficient, drag coefficient, and lift to drag ratio were compared for seven different airfoils through the range of angle of attack between -3 and 15 degrees. MH114 airfoil section fulfilled the criteria of the selection approach and showed the overall best performance at the specifications of the design thus, it has been selected for the wing airfoil section. Moreover, the flow physics of the chosen airfoil MH114 have been examined in detail.

Keywords: Aerodynamic analysis, optimization, airfoil, unmanned aerial vehicle

İNSANSIZ HAVA TAŞITI KANADININ CFD KULLANARAK OPTİMİZASYONU VE AERODİNAMİK ANALİZİ

ÖZ

Kanat, uçak tasarımının performansını ve verimliliğini doğrudan ve önemli ölçüde etkileyen temel bir parçasıdır; bu nedenle tasarım sürecinin uçak kanadı seçimi kısmı, tüm uçak tasarım sürecinin başarısını etkileyen önemli bir adımdır.

Bu tez çalışmasında, küçük insansız hava aracının kanat seçimi yapılmıştır. İnsansız hava taşıtlarının popülaritesi ve uygunluğuna dayalı belirlenen yedi farklı kanatçık SA7035, SA7038, SD7090, MH45, MH114, MH32 ve MH60'tan optimum kanat profilini belirlemek üzere iki boyutlu hesaplama simülasyonu yapılmıştır. Simülasyonlar, sonlu hacimler yöntemi kullanılarak ANSYS Fluent'te düşük akson Reynolds akışında $Re= 2.4 \cdot 10^5$ düşük ses altı akış hızında gerçekleştirilmiştir. Geçiş (γ-Reθ) SST modeli türbülans modeli olarak kullanılmıştır. XFOIL kullanılarak Fluent sonuçlarını doğrulamak için bir karşılaştırma da yapılmıştır.

Kaldırma/sürükleme oranı, kaldırma katsayısı, düşük durma hızı ve bazı durma özellikleri, tasarım gereksinimlerini karşılayan uygun bir kanat profili seçmek için kullanılan kriterler olarak belirlenmiştir. Kaldırma katsayısı, sürtünme katsayısı ve kaldırma sürtünme oranının aerodinamik özellikleri, hücum açısı aralığında -3 ile 15 derece arasındaki yedi farklı kanat profili için karşılaştırılmıştır. Seçim yaklaşımının kriterlerini yerine getirmiş ve tasarım şartnamelerinde en iyi performansı göstermiş olan MH114 kanat profili bu tasarımın kanat profili olarak seçilmiştir. Ayrıca, seçilen kanatçık MH114'ün akış fiziği detaylı olarak incelenmiştir.

Anahtar Kelimeler: Aerodinamik analiz, optimizasyon, kanat profili, insansız hava aracı

CONTENTS

M.Sc. THESIS EXAMINATION RESULT FORM ii
ETHICAL DECLARATION iii
ACKNOWLEDGMENTS iv
ABSTRACT v
ÖZ vi
NOMENCLATURE ix
LIST OF TABLES xi
LIST OF FIGURES xii

CHAPTER 1 - INTRODUCTION 1
1.1 Literature Review 2
1.1.1 A Brief History of Airfoils 2
1.1.2 Studies about UAVs Airfoils 4
1.2 Aim of the Study 9

CHAPTER 2 - AIRFOIL AERODYNAMIC CHARACTERISTICS 10
2.1 Airfoil Nomenclature 10
2.2 Aerodynamic Forces 11
2.2.1 Lift Force 11
2.2.2 Drag Force 11
2.3 Airfoil Characteristics 11
2.4 Pressure Distribution 12
2.5 Airflow over Airfoil 12
2.6 Laminar Separation Bubbles 13
2.7 Airfoil Selection 14

CHAPTER 3 - METHODOLOGY 15
3.1 The Unmanned Air Vehicle 15
3.1.1 Conceptual Design 15
3.1.2 Preliminary Design 15
3.2 Numerical Analysis 17
3.2.1 Geometry Modeling 17
3.2.3 Numerical Setup 27

CHAPTER 4 - SIMULATION RESULTS AND DISCUSSION 35
4.1 Airfoil Selection Criteria 35
4.2 Lift Coefficient,C_l 37
4.3 Drag Coefficient, C_d 38
4.4 Lift-to-Drag Ratios, C_l/C_d 39
4.5 Flow Field Analysis for MH114 40
4.5.1 Contour of Intermittency 40
4.5.2 Contour of Pressure 41
4.5.3 Coefficients of Pressure 42
4.5.4 Contour of Velocity 44
4.5.5 Streamlines of Velocity 45
4.5.6 Turbulent Kinetic Energy Distribution 50
4.6 Comparison of Fluent and XFOIL Results 52

CHAPTER 5 - CONCLUSIONS 56

REFERENCES 58

CURRICULUM VITAE 61

NOMENCLATURE

Acronyms

c	Chord length
C_d	Airfoil drag coefficient
C_l	Airfoil lift coefficient
C_l/C_d	Lift to drag ratio
C_m	Airfoil moment coefficient
C_f	Skin friction coefficient
C_{l_i}	Wing airfoil ideal lift coefficient
$C_{l_{stall}}$	Wing airfoil lift coefficient at stall speed
C_{L_c}	Aircraft ideal cruise lift coefficient
$C_{L_{c_w}}$	Wing cruise lift coefficient
CFD	Computational Fluid Dynamics
HAUAV	High-Altitude Unmanned Aerial Vehicle
L	Reference length, m
LSB	Laminar separation bubbles
NACA	National Advisory Committee for Aeronautic
RAF	Royal Aircraft Factory
RANS	Reynolds-Averaged Navier–Stokes
Re	Reynolds number
SST	Shear Stress Transport
SUAV0	Small Unmanned Aerial Vehicle
TKE	Turbulent Kinetic Energy
U	Velocity, m/s
u_*	Friction velocity, m/s
UAS	Unmanned Aircraft System
UAV	Unmanned Aircraft Vehicle
U.S.A.	United States of America
W	Weight of UAV
WSM	Weighted Scoring Method

Greek Letters

α	Angle of attack
δ	Laminar boundary layer thickness, m
μ	Dynamic viscosity, kg/ (m·s)
ν	Kinematic viscosity, m^2/s
ρ	Freestream density, kg/m^3
τ_ω	Wall shear stress, Pa

LIST OF TABLES

Table 3.1 Small unmanned aerial vehicle specifications 15

Table 3.2 Global mesh parameters 19

Table 3.3 Inflation parameters 20

Table 3.4 Edge sizing parameters 21

Table 3.5 Body sizing parameters 22

Table 3.6 Mesh refinement values 26

Table 3.7 Fluent launcher settings 27

Table 3.8 Solver general settings 28

Table 3.9 Viscous model settings 29

Table 3.10 Fluid parameters 29

Table 3.11 Boundary conditions 30

Table 3.12 Reference values 31

Table 3.13 Areas of airfoils 31

Table 3.14 Solution methods 32

Table 3.15 Solution controls 32

Table 4.1 Criteria for flying wing airfoil selection. 36

Table 4.2 C_l/C_d for all the airfoils at α =0 39

LIST OF FIGURES

Figure 1.1 Double-surface airfoil sections by Phillips 2

Figure 1.2 RAF 6 airfoil..... 3

Figure 1.3 USA 6 airfoil 3

Figure 1.4 Typical airfoils..... 4

Figure 1.5 Optimal and initial aifoil shapes..... 5

Figure 1.6 Shape of airfoils of different relative thickness values 6

Figure 1.7 Shape of airfoils at different locations with maximum relative thickness 6

Figure 1.8 E420 High lift airfoil 7

Figure 1.9 TL54 Airfoil type 8

Figure 1.10 MH 114, SA7025, SA7035, SA7038, SA7090 airfoil types 8

Figure 2.1 Airfoil nomenclature 10

Figure 2.2 Typical airfoil pressure distribution 12

Figure 2.3 Airflow over an airfoil 13

Figure 2.4 Features of a laminar separation bubble flow 14

F**igure 3.1** Airfoils' profiles 16

Figure 3.2 C-domain around the airfoil..... 18

Figure 3.3 Inflation mesh around the airfoil 21

Figure 3.4 Edge sizing with bias factor..... 22

Figure 3.5 Elements growing gradually in body sizing 23

Figure 3.6 Skewness 24

Figure 3.7 Skewness mesh metrics spectrum 24

Figure 3.8 Different mesh sizes from course to fine..... 25

Figure 3.9 Mesh convergence curve 26

Figure 3.10 Scaled residuals history of transient solver is converged 34

Figure 4.1 Cl- α curves of the airfoils 37

Figure 4.2 Cd- α curves of the airfoils 38

Figure 4.3 Cl/Cd- α curves of the airfoils 39

Figure 4.4 Contour of intermittency for different α (-3°, 0°, 3°, 6°, 9°, 12°, 15°) degrees 40

Figure 4.5 Contour of pressure for different α (-3°, 0°,3°, 6°, 9°, 12°, 15°) degrees 41

Figure 4.6 Pressure coefficient profiles for different α (-3°, 0°,3°, 6°, 9°, 12°, 15°) degrees 43

Figure 4.7 Contour of velocity for different α (-3°, 0°,3°, 6°, 9°, 12°, 15°) degrees 44

Figure 4.8 Velocity streamlines near the trailing edge at different α (-3°, 0°, 3°, 6°, 9°, 12°, 15°) degrees 46

Figure 4.9 Velocity streamlines in the suction surface of the airfoil at different α (-3°, 0°, 3°, 6°, 9°, 12°, 15°) degrees..... 48

Figure 4.10 Contour of turbulent kinetic energy for different α (-3°, 0°, 3°, 6°, 9°, 12°, 15°) degrees 51

Figure 4.11 Lift and drag coefficient graphs for XFOIL and Fluent for the airfoils HS520, MH114, MH45, MH60, SA7035, SA7038, and SD7090 at α (-3°, 0°, 3°, 6°, 9°, 12°, 15°) degrees 53

CHAPTER 1

INTRODUCTION

According to the technology developments over the recent years, the interest in developing unmanned aircraft systems (UAS) have rapidly increased; thus, the studies of unmanned aerial vehicles (UAVs) have kept growing at very fast rate also. UAV is an aircraft with no pilot on board. It can be autonomous or controlled remotely from the ground for different purposes and can generally be divided into two types: fixed-wing aircraft and rotorcraft. The size of it differs according to the purpose of its use for military and civil applications. Small-scale UAVs are designed for different purposes in scientific research, while in the area of civil applications it can be used in cases like emergency monitoring, aerial filming, geological survey, and fire detection, it can be also an ideal choice in warfare and defense for collecting information with zero injury [1].

Small unmanned aerial vehicle (SUAV) refers to the class of fixed-wing aircraft with a wing span between 1.5 m and 3 m, which further can be categorized into small tactical, miniature, and micro UAVs. The miniature unmanned aircrafts have wing span less than 1.5 m. Typical small fixed unmanned aircrafts can be hand launched or launched with assistance of a pneumatic launch device. Automatic landing can be achieved via a parachute, a controlled glide slope or a deep stall therefore it does not require a runway for takeoff or landing. Also, it can be flown between 30 m and 1200 m altitude above the ground level, battery powered operates from 20 minutes to several hours at flight speed between 10 m/s and 50 m/s, payloads range from grams to several kilograms [2, 3].

The design principles for UAVs are like the principles developed and used for the design of commercial aircrafts. A sensible chosen of wing airfoil is a very significant part of the aerodynamic design process for UAVs. The chosen airfoil predetermines basically the performance of the designed UAV. For this reason, it is important for more attention to be paying to the problem of an UAV wing airfoil selection based on

specific properties for UAVs. In flights at low flow speed to obtain the lift of a particular airfoil at a certain angle of attack α, aerodynamicists for more than 100 years have been measuring the properties of an airfoil experimentally in low-speed wind tunnels. The properties of an airfoil have been also calculated theoretically by applying one of the approaches: low-speed airfoil theory, the analytical thin airfoil theory or the numerical panel method. Since the 1960s, the development of the high-speed computers has given the opportunity for numerical solution methods to take a notable place in solving aerodynamic problems. Nowadays, the suitable design of airfoil sections is more important than ever. Using modern airfoil design computer programs using either panel techniques or direct numerical finite-difference solutions of the governing partial differential equations for the flow field, the airfoil shapes can be designed for new designs of aircrafts and shaped in way to fulfill the design requirements [4].

1.1 Literature Review

1.1.1 A Brief History of Airfoils

In 1884, Horatio F. Phillips developed a series of double-surface, cambered airfoils. Figure 1.1 shows Phillip's airfoil sections.

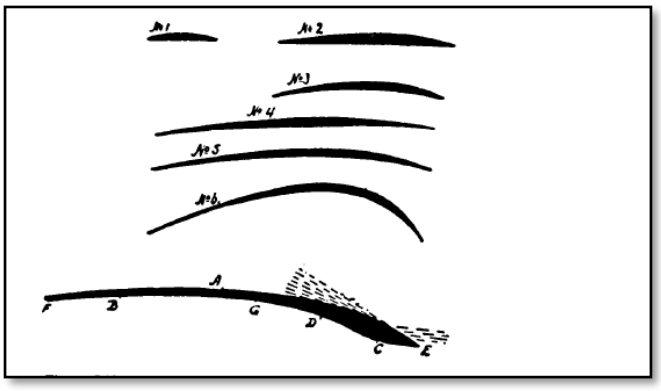


Figure 1.1 Double-surface airfoil sections by Phillips [5]

Wright Brothers tested several hundred different airfoil shapes between 1901-1902 and from their experimental results they chose an airfoil with a 1/20 maximum camber to chord ratio for their successful Wright Flyer I in 1903.

The series of Royal Aircraft Factory (RAF) airfoils used in the World War I airplanes. Figure 1.2 illustrates the shape of the RAF 6 airfoil.

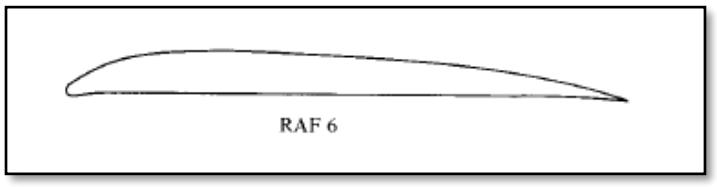


Figure 1.2 RAF 6 airfoil [5]

The first systematic series organized and studied by the National Advisory Committee for Aeronautic (NACA) were the United States of America (U.S.A) airfoil section series. Figure 1.3 represents the shape of USA6 airfoil [5].

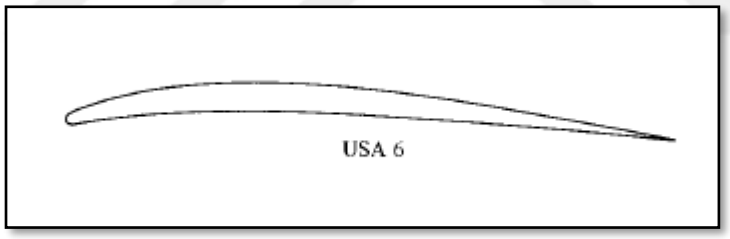


Figure 1.3 USA 6 airfoil [5]

1.1.1.1 Airfoil Families

In Figure 1.4, a variety of airfoils are shown, most of the old airfoils were developed by trial and error. In the 1930's, four-digit airfoils have been developed by the NACA which is defined mathematically. They are hardly used these days for wing design except for the uncambered four-digit airfoils still widely used for design of tail surfaces for subsonic aircraft. Then the NASA five-digit airfoils were improved to achieve greater maximum lift by moving the position of maximum camber forward in the direction of the leading edge. The six-series airfoils are still being used as a starting

point for high-speed-wing design which were designed to reduce drag effects by increasing the laminar flow on the upper surface of the airfoil. These days the custom-designed wing airfoil sections have being really popular with the developments of the computational airfoil design. Modern airfoil design is based upon inverse computational solutions for desired pressure (or velocity) distributions on the airfoil.

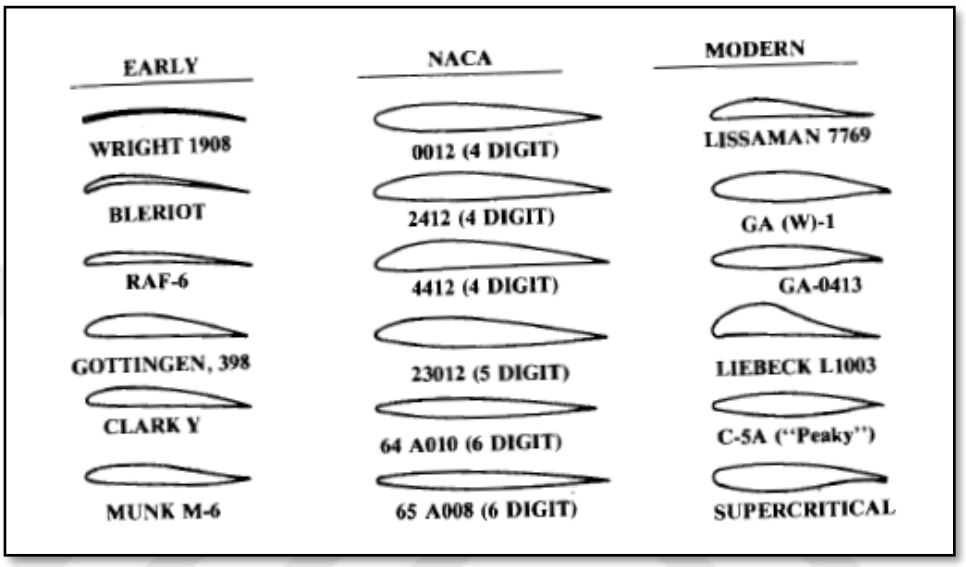


Figure 1.4 Typical airfoils [6]

1.1.2 Studies about UAVs Airfoils

D.N. Srinath and Sanjay Mittal used a continuous adjoint method for the design of airfoils. Figure 1.5 illustrates the initial and optimal airfoil shapes of the study. To determine optimal airfoil shape in unsteady viscous flow at chord Reynolds number $Re=1 \cdot 10^4$, they used the maximum lift, the minimum drag and the minimum ratio of drag to lift as the criteria to obtain the optimal shape of the airfoil. Starting from NACA0012 airfoil as a premier guess for the calculations. The optimal airfoils of that study were thin, with the largest thickness to chord ratio 5.4%. The aerodynamic performance of those airfoils was compared to a NACA 0012 airfoil and is found that they produce more than six times more lift which is a result of a strong suction peak, mild adverse pressure gradient on a major length of the upper surface and a large high-pressure region on the lower surface. Quite large value of the time-averaged ratio of

lift to drag (~17.8) is obtained as a result of minimization of the ratio of drag to lift results in an airfoil. The flow remained attached for close to 70% of the chord length while minimizing the time-averaged drag coefficient [7].

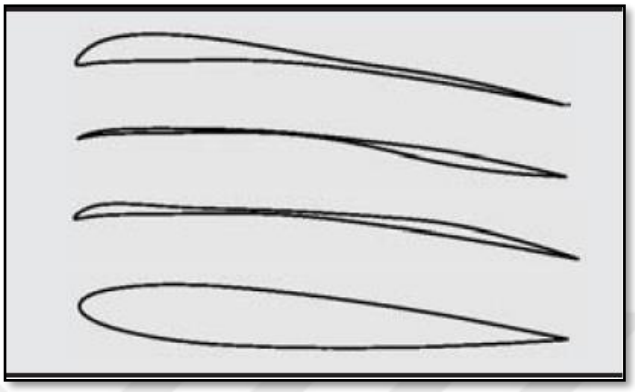


Figure 1.5 Optimal and initial airfoil shapes [7]

Ma Dongli, Zhao Yanping, Qiao Yuhang, Li Guanxiong carried out aerodynamic simulation on the flow over many airfoils of High-Altitude Unmanned Aerial Vehicles (HAUAVs) cruising at a low speed and investigated the features of low Reynolds number flow. They explored the effect of the relative thickness of airfoil and the positions of the maximum relative thickness on aerodynamic performance. Figures 1.6 and 1.7 represent airfoil shapes of different relative thickness values and airfoils at different locations with maximum relative thickness, respectively. In the study they found that the relative thickness value in the low Reynolds number regime affects the position and magnitude of the laminar separation bubble. Thus, to obtain fine performance the amount of maximum relative thickness ought to be very small. In addition, the position of the maximum relative thickness should be closer to the trailing edge to achieve the equilibrium of drag, lift-drag ratio and stall characteristics. Also, they made an experimental study which verified the validity of the numerical method [8].

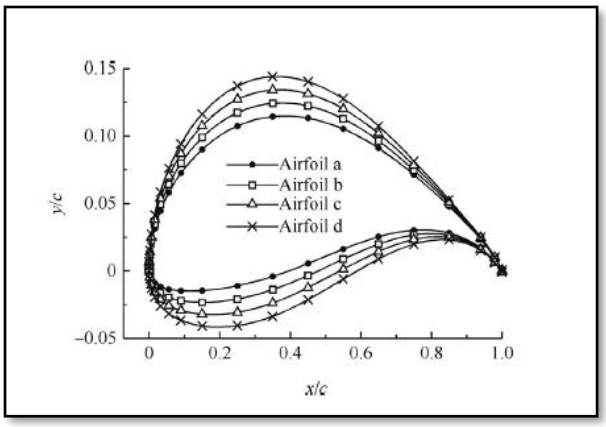


Figure 1.6 Shape of airfoils of different relative thickness values [8]

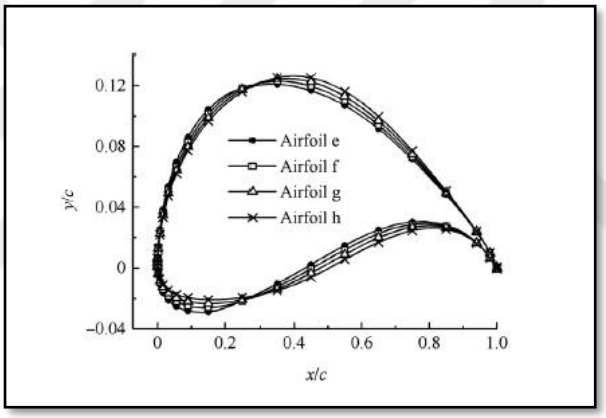


Figure 1.7 Shape of airfoils at different positions with maximum relative thickness [8]

Spyridon G. Kontogiannis a, John A. Ekaterinaris have made a design study for a small size light UAV then built the model and tested it in flight in order to fulfill the growing needs of light UAV aircrafts for aerial photography and surveillance purposes. For the first configuration of the design in the conceptual study different relations were developed. In the preliminary design stage, some analysis has been performed to predict the stability and aerodynamic performances. They have evaluated the aerodynamic characteristics and the efficiency of the airfoil section, the wing, and the full configuration using Computational Fluid Dynamics (CFD). Through the choosing procedure of the airfoil shape the X-Foil code was used. The airfoil section which preferable matches the demands of the UAV is distinguished by high camber and high-

pressure gradient along its chord, which is the E420 high lift airfoil shown in Figure 1.8. To reduce the form drag, a computational optimization study was carried out. Moreover, some enhancements were implemented to the wingspan for optimization the aerodynamic efficiency in order to improve the aerodynamic efficiency of the whole configuration [9].

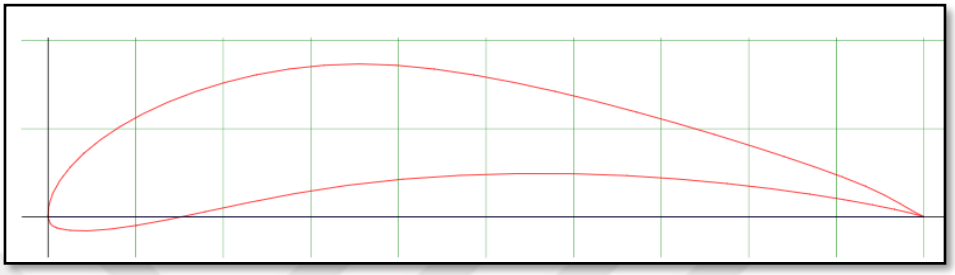


Figure 1.8 E420 High lift airfoil [10]

Anastasios P. Kovanis, Vangelis Skaperdas, John A. Ekaterinaris designed, constructed, and tested in flight a light cargo unmanned air vehicle (UAV). In the preliminary phase, the basic aerodynamic analysis which was based on Navier-Stokes equations for the wing, the wing-body configurations and the stability analysis which was based on the linearized theory were presented. At the preliminary design phase, they performed different numerical simulations for the airfoil. In the designed model there were no lift enhancement devices to meet some manufacturing and cost considerations, so the coefficient of lift was for the cruising phase. The flow was counted as fully turbulent and the Eppler 420 airfoil was eventually selected. The propulsion system was carefully selected. Furthermore, by using CFD simulation for the whole configuration, aerodynamics enhancements were achieved [11].

Ngo Khanh Hieu, Pham Quang Vinh, Dinh Anh Bao designed and analyzed the configuration of a small UAV combined between a flying-wing and a quadrotor based on the performance at its cruise speed. In the research they used XFRL5, a multi-fidelity analysis tool. Weighted Scoring Method (WSM) was used to select the suitable airfoil at the Reynolds number (Re) which is about $3 \cdot 10^5$. According to the design requirements and the criteria for each parameter, TL54 represented in Figure 1.9 had

maximum weighted score and was chosen for the UAV flying-wing in the regime of forward flight among 29 airfoils [12].

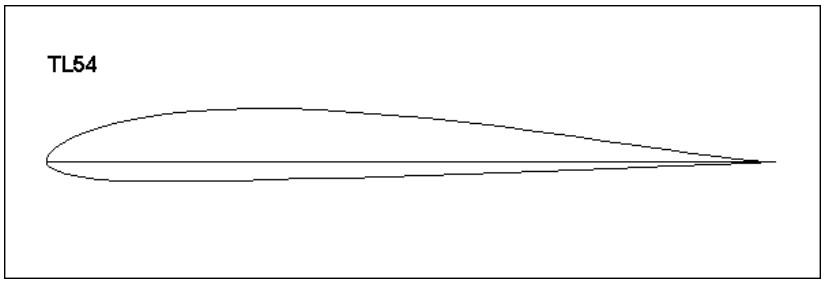


Figure 1.9 TL54 Airfoil type [13]

In the research of Ugur C. Yayli, Cihan Kimet, Anday Duru, Ozgur Cetir, Ugur Torun, Ahmet C. Aydogan, Sanjeevikumar Padmanaban and Ahmet H. Ertas, a small UAV have been designed, made, simulated and tested in flight to meet the requirements of shorter take-off distance and a higher flight speed. The airfoil was selected considering aerodynamic characteristics. Using XFLR-5 analysis tool, SA7025, SA7038, SA7035, SD7090, MH 114 airfoils were analyzed. The profiles of these airfoils represented in Figure 1.10. A lift-to-drag ratio C_l/C_d is calculated to compare various scenarios which have operated at low Reynolds numbers Re= $4 \cdot 10^5$ and it has been found that MH 114 has the best results, so it would be the best choice for the designed aircraft [14].

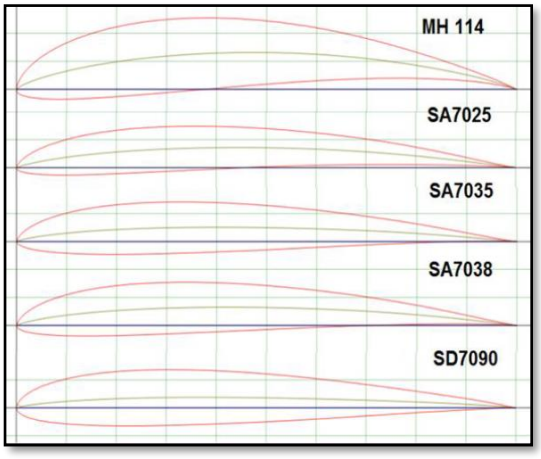


Figure 1.10 MH 114, SA7025, SA7035, SA7038, SA7090 airfoil types [14]

1.2 Aim of the Study

The purpose of this thesis is to select an appropriate wing airfoil profile for a SUAV operating at a low chord Reynolds number which can be used for different applications such as observation boarding security and forest fire control.

For such studies the designer can design the airfoil based on the desirable pressure or velocity distribution using inverse computational solutions or can perform experimental or numerical study for some airfoils then select the one which satisfies the design requirements. In this study it has been planned to perform CFD simulations for some airfoils and select the one which matches the selection criteria.

The first step in accomplishing this purpose is to properly pick airfoils for SUAV operating at a low Reynolds number. The next step will be to perform computational simulations for these airfoils and examine the results to choose the convenient airfoil profile for the design.

CHAPTER 2

AIRFOIL AERODYNAMIC CHARACTERISTICS

2.1 Airfoil Nomenclature

Airfoil nomenclature is shown in Figure 2.1, and their definitions are in the following:

Mean camber line: the points halfway between the upper and lower surfaces of the airfoil.

Leading and trailing edges: The most forward and rearward points of the mean camber line.

Chord line: the straight line connecting the leading and trailing edges.

Chord *c*: the specific distance from the leading to the trailing edge measured along the chord line.

Camber: the maximum distance between the mean camber line and the chord line.

Thickness: is the distance between the upper and lower surfaces of the airfoil.

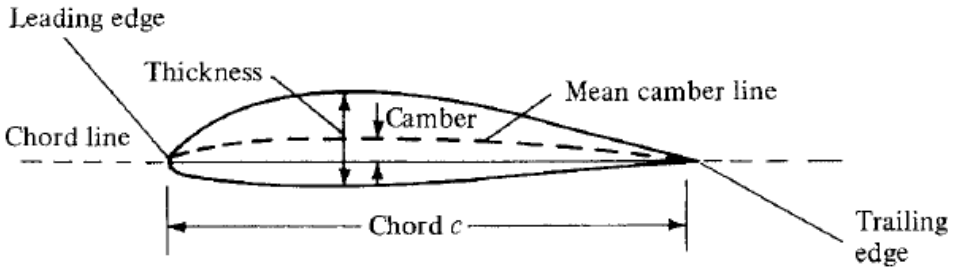


Figure 2.1 Airfoil nomenclature [4]

2.2 Aerodynamic Forces

2.2.1 Lift Force

The air moves over the wing top surface with more speed than its velocity on the bottom surface and according to that the lifting force of an aircraft can be created and that is happened by the wing's angle of attack and/or wing camber. When the local velocity of the air raises, the dynamic pressure raises and consequently the static pressure must decrease according to Bernoulli's equation. The top airfoil surface has lower pressure than ambient pressure which works to draw the airfoil up while the bottom airfoil surface gains lower - than - ambient pressure which works to push the airfoil upward. Thus, the net lifting force is generated by the integrated differences in pressure between the upper and lower surface of the airfoil [6].

2.2.2 Drag Froce

The drag force of an airfoil is a two-dimensional drag and is called profile drag. It is a combination of the skin-friction drag and the viscous separation drag. The skin-friction drag depends upon the wetted area, the smoothness of the surface and on the characteristics of the boundary layer flow and the value of the skin friction is less in the laminar than its value in the turbulent boundary layer. While the viscous separation drag also called "form drag," is an effect of the flow separation of the boundary layer on the airfoil. The form drag depends upon the position of the separation point on the airfoil. If the flow separates nearer to the front of it the drag is much higher than if it separates more towards the rear. The location of the separation point depends upon the airfoil's camber and is affected by the amount of energy in the flow. However, the profile drag increases as the angle of attack α is increased [6].

2.3 Airfoil Characteristics

In order to conveniently accomplish both forces, two basic airfoil characteristics need to be determined carefully through the design/selecting process of the airfoil of an aircraft. These both characteristics are the lift coefficient and the drag coefficient. They

depend on the shape of the airfoil as well as Reynolds number and change with the changes of the angle of attack. The convenient way of describing the aerodynamic characteristics of an airfoil section is to plot the values of the lift coefficient C_l , the drag coefficient C_d, the ratio of lift to drag L/D, and the position of the centre of pressure, or the pitching moment coefficient C_m against the angle of attack [15].

2.4 Pressure Distribution

Figure 2.2 shows pressure distribution over an airfoil. It presents the typical distributions for the upper and lower surfaces at subsonic speeds. The reducing in pressure on the top surface is greater than the raising on the bottom surface. Both the low pressure on the top surface and the high pressure on the bottom surface is most noticeable over the front part of the airfoil. That means the upper surface of an airfoil provides the greater fraction of the lift [15].

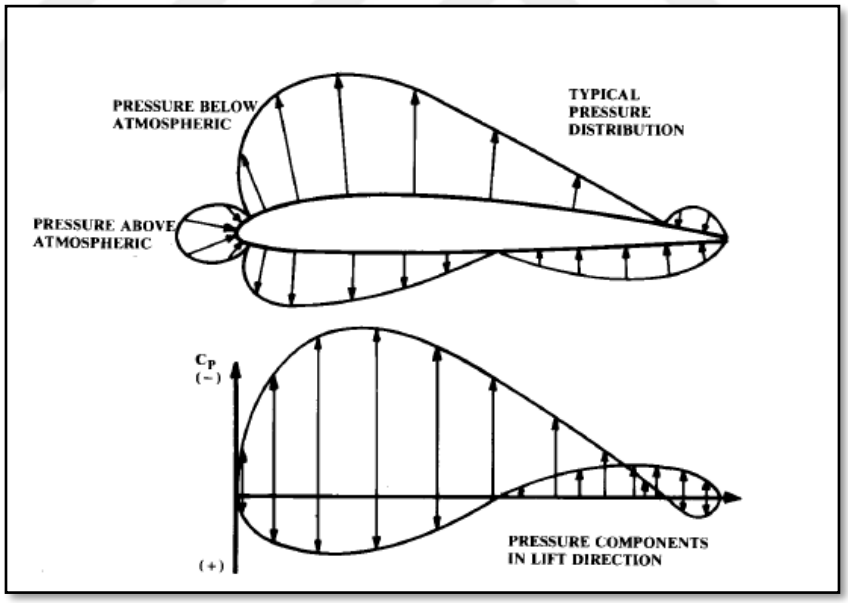


Figure 2.2 Typical airfoil pressure distribution [6]

2.5 Airflow over Airfoil

The flow of the air over a typical airfoil has special properties. As the air flows towards an airfoil it's noticed that there is a little upflow before arriving the airfoil. Then the air

does not strike on the nose but splits at a point just behind it on the airfoil lower surface, the streamlines are nearer together on the area upper the airfoil where the pressure is low and there is a downflow after passing the airfoil. Figure 2.3 shows typical airflow over an airfoil [15].

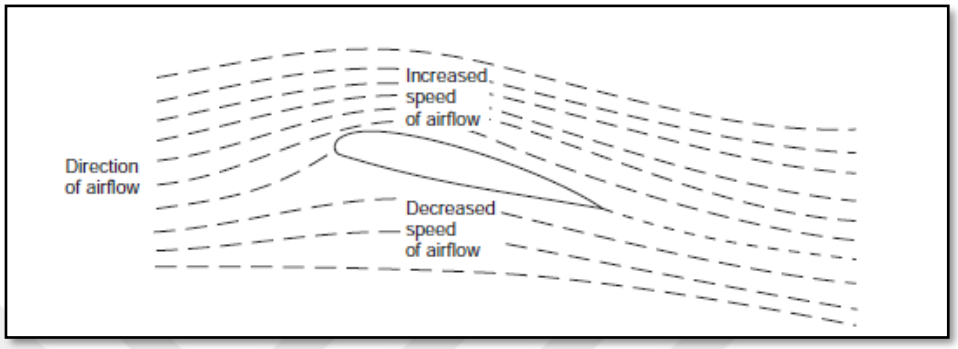


Figure 2.3 Airflow over an airfoil [15]

2.6 Laminar Separation Bubbles

The phenomena of laminar separation bubbles (LSBs) or a leading-edge separation happens in applications involve low Reynolds number flows in range of 10^4 to 10^6 with large pressure gradients. In such cases the effect of viscous force is dominant and the LSB may rise some passive effects like decreasing on the lift force, increasing on the drag force which thus have reverse effects on the aircraft performance. The position and magnitude of the separation bubbles are functions of the airfoil profile, the angle of attack, Reynolds number, the freestream disturbances and the turbulence intensity [16, 17]. The separation and formation of a laminar separation bubble on the upper airfoil surface is due to the adverse pressure gradient generated because of the airfoil's curvature which is in other words resistance of the boundary layer to make a natural transition from laminar to turbulent flow on the airfoil surface [18]. The main features of the laminar separation bubble are illustrated in Figure 2.4 [19].

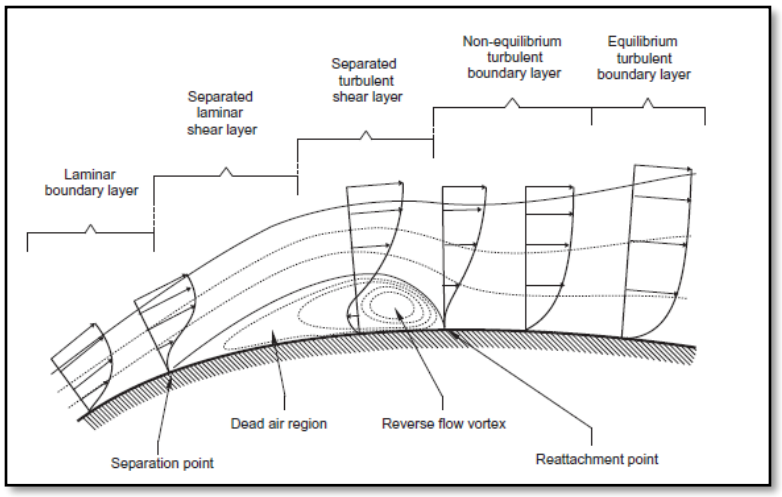


Figure 2.4 Features of a laminar separation bubble flow [20]

2.7 Airfoil Selection

The heart part of the aircraft is the airfoil because of its effects on many characteristics of the flight like cruise speed, stall speed, take off, handling qualities, landing distances and overall aerodynamic efficiency. The choice of the best airfoil section depends upon the speed and the size of the airplane. It calls scale effect the Reynolds number. The best airfoil section for a light low speed aircraft will be different than the best airfoil section for a large fast airplane [6].

CHAPTER 3

METHODOLOGY

3.1 The Unmanned Air Vehicle

3.1.1 Conceptual Design

During the conceptual design stage, specifications, limitations and weight estimation of the SUAV are set. The purpose of this SUAV with capability of carrying modern photography and video equipment is to supply observation services like boarding security, forest fire control and agricultural applications for social benefits. In order to guarantee good quality photos and filming, the stalling speed was kept down to low levels. The weight of the aircraft itself, the electronic and video equipment do not exceed a total weight of 7 kg. Its technical and physical specifications are presented in Table 3.1.

Table 3.1 Small unmanned aerial vehicle specifications

SUAV specifications	Value
Weight	7 kg
Max altitude	1200 m
Endurance	45 min
Cruise speed	13 m/s
Cruise α	0 deg
Chord length	0.280 m
Stalling speed	8 m/s
Wing planform area	0.420 m^2

3.1.2 Preliminary Design

When developing a fixed wing aircraft, one of the most important decisions is airfoil selection. The large drag and low lift to drag ratio values are related to viscous effects which are relatively large at low Re. A random choosing of airfoils to carry out the study at low Reynolds numbers is inappropriate because the conventional airfoils designed for high Reynolds numbers have been found to have a nonoptimal

performance at low Re. Thus, to get acceptable aerodynamic performance the airfoils of this study were picked based upon the literature survey. Seven different airfoil profiles were selected to carry out the numerical analysis which have been used in studies of SUAV operating at low Re. Figure 3.1 represents the profiles of the selected airfoils.

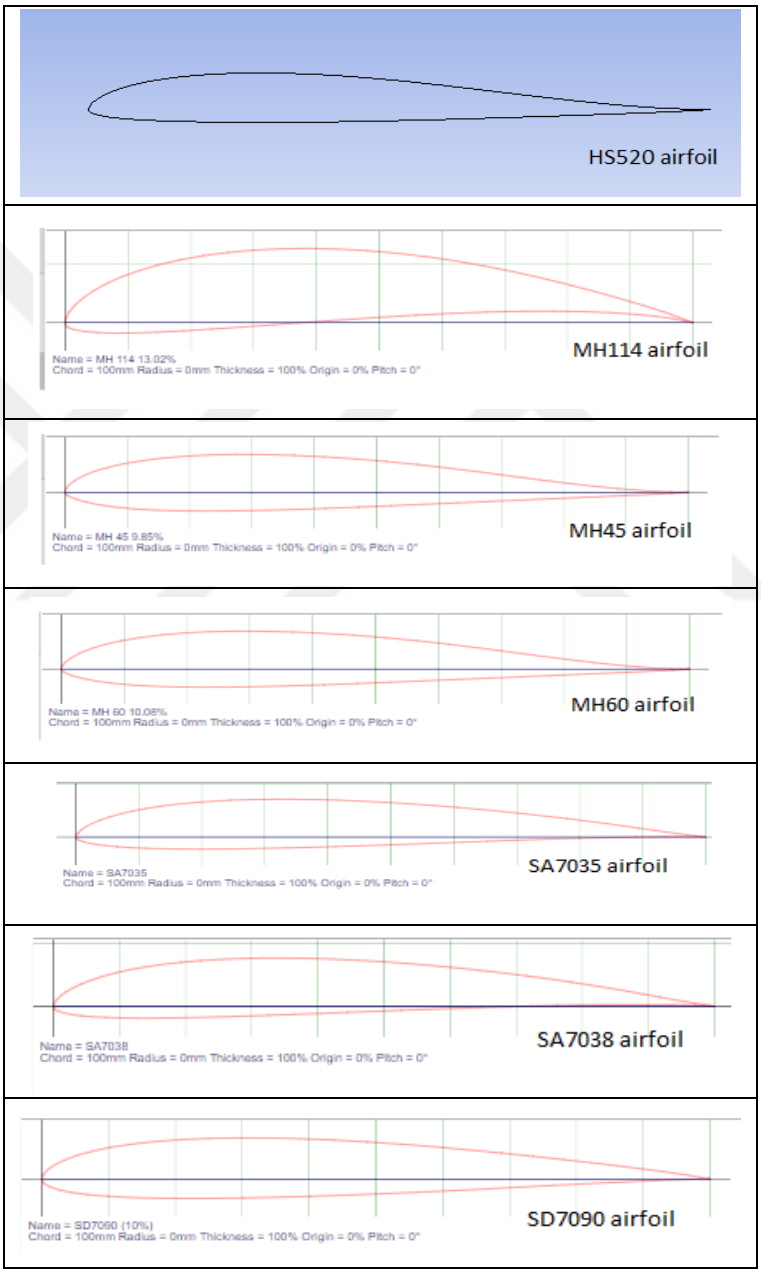


Figure 3.1 Airfoils' profiles [10]

3.2 Numerical Analysis

Extensive previous works have proved the accuracy and effectiveness of numerical methods. Numerical analysis consists of 3 parts: pre-processing (geometry generation and meshing), solution (problem specifications and numerical computation) and post processing parts.

3.2.1 Geometry Modeling

3.2.1.1 Airfoil Data Pre-processing

The airfoils data points have been taken from Airfoil Tools website then formatted and imported into Design Modeler software available in the ANSYS package. Airfoil geometries were created and scaled to have chord length c = 280 mm.

3.2.1.2 Domain Definition

ANSYS Design Modeler was used to create flow domain, a control volume around the airfoil where the air will flow is generated big enough to predict correctly the probable pressure field around the airfoil. To set the domain two different volumes were defined. The outer one is to determine the essential domain while the interior one consists of two parts: the small circle around the airfoil and the rectangle covers the region behind the airfoil. The interior regions have been used in body sizing for providing smaller cells around the airfoils. Then regarding create enclosure volume around the geometric models, the airfoil models were subtracted from the two volumes. To obtain better results, C-type enclosure volume was chosen. The domain is extended 15c in front of the airfoil where the inlet boundary was set and 20c behind the airfoils where the outlet boundary was set and 15c above and below the airfoil. The fluid domain around the airfoil is shown in Figure 3.2.

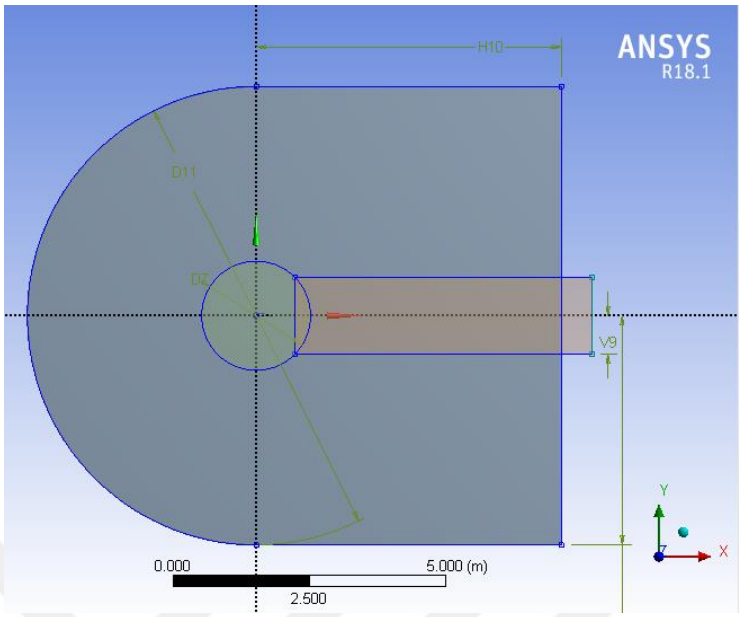


Figure 3.2 C-domain around the airfoil

3.2.2 Grid Generation

To obtain accurate results the mesh should met the following requirements:

a. y+=1
b. Adequate improved element in the leading and trailing edge
c. Adequate improved element in the downstream flow over the airfoil.

Generally, to avoid the divergence caused by rough grid the structured grid is preferable than unstructured one. However, due to computer power limitations a hybrid mesh is generated for this study. The domain is filled with an unstructured triangle mesh except for the area near the airfoil surface the cells were structured. In low Reynolds number flows, numerical simulation needs fine computational grid. A body of influence approach is used to discretize the domain into various zones. The mesh density is coarse in the zone around the boundaries of the domain then it is refined as mesh goes towards the surface of the airfoil where the density of mesh become higher in this zone. The C-type mesh was generated by ANSYS Meshing.

As an advanced size function, proximity and curvature function was chosen based on that the geometric model has curvature shape. The relevance option allows the

program to control the fineness of the mesh for the entire model. Relevance center was set to fine. During the meshing process to capture curvature regions (leading edge) smoothly, curvature normal angle was kept as its default value 18°. Minimum and maximum size parameters were set considering the chord length of the airfoil that maximum size was specified to 250 mm and the minimum size was set to 50 mm. Smoothing was adjusted to high to increase the element quality by building the cells in the mesh with respect to surrounding other elements. Table 3.2 represents the global mesh parameters.

Table 3.2 Global mesh parameters

Advanced size function	Proximity and curvature
Relevance center	Fine
Curvature normal angle	18°
Min size	50 mm
Max face size	250 mm
Smoothing	High

3.2.2.1 Inflation

In order to capture the separation bubble and the boundary layers the y plus value need to be ensured to be equal or less than one. In low Reynolds simulation of the flow around an airfoil y^+ can be approximately set to one and calculate the first layer wall distance according to formula 3.6 [21].

Reynolds Number Calculation

$$Re = \frac{U\,L}{\upsilon} = \frac{\rho\,U\,L}{\mu} \tag{3.1}$$

Schlichting skin-friction correlation

$$C_f = [\,2\,log_{10}(Re_x) - 0.65]^{-2.3} \quad \text{for} \quad Re < 10^9 \tag{3.2}$$

Wall shear stress

$$\tau_\omega = C_f \;\frac{1}{2}\;\rho\,U^2_{freestream} \tag{3.3}$$

Friction velocity

$$u_* = \sqrt{\frac{\tau_\omega}{\rho}} \tag{3.4}$$

Wall distance

$$y = \frac{y^+ \mu}{\rho u_*} \tag{3.5}$$

According to equations above, at chord Reynolds number Re= $2.4 \cdot 10^5$estimated first layer wall distance is $2.48 \cdot 10^{-5}$ m. Then, to determined laminar boundary layer thickness formula 3.6 has been used in the study [4].

$$\delta = \frac{5.0x}{\sqrt{Re_x}} \tag{3.6}$$

Using first layer thickness for inflation option and a value of growth rate equals 1.2, maximum layers are found 18 layers to reach the calculated total thickness. Maximum layers value was taken 25 to ensure the good covering of the boundary layers around the airfoil. Figure 3.3 shows the inflation around the airfoil and its parameters are in Table 3.3.

Table 3.3 Inflation parameters

Scoping method	Geometry selection
Geometry	1face
Boundary scoping method	Geometry selection
Boundary	2edges
Inflation option	First layer thickness
First layer height	$2.48 \cdot 10^{-5}$ m
Maximum layers	25
Growth rate	1.2
Inflation algorithm	Pre

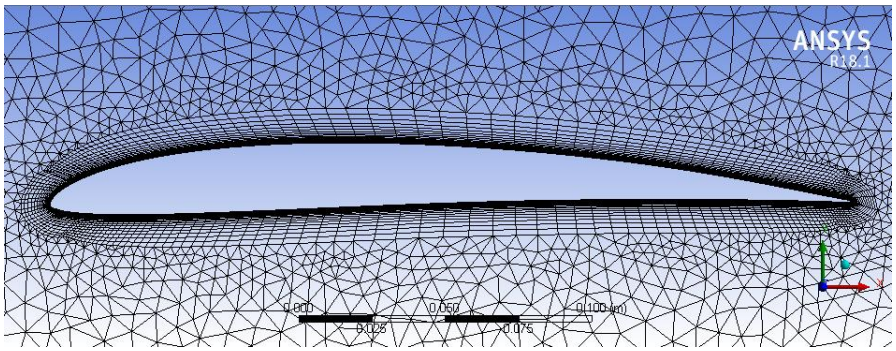


Figure 3.3 Inflation mesh around the airfoil

3.2.2.2 Edge Sizing

Element size value was set to 2 mm and behavior was set to soft which help to create fine cells at curved sides. To get smaller elements at leading and trailing edge, bias type sizing is used as shown in Figure 3.4. Smooth transition was used as a bias option and growth rate was reduced to 1.04 so the elements grow in small increasing of the value from the leading and trailing edges towards the middle of the airfoil section. Edge sizing parameters are presented in Table 3.4.

Table 3.4 Edge sizing parameters

Scoping method	Geometry selection
Geometry	2 edges
Type	Element size
Element size	$2 \cdot 10^{-3}$ m
Behavior	Soft
Bias type	- -- --- ---- --- -- -
Bias option	Smooth transition
Bias growth rate	1.04

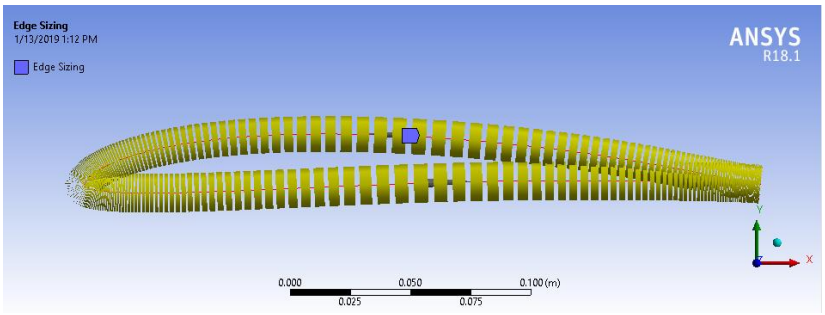


Figure 3.4 Edge sizing with bias factor

3.2.2.3 Body Sizing

The number of elements in the mesh plays a significant role in the calculation time thus the cost of the simulation. To run the simulation in shorter time without influencing the accuracy of the results it is important to define different zone in the domain considering the properties of the model in order to set different element size in these zones. Body sizing function was used to get smaller elements in the zones around the airfoil that the element size was set to 0.01 m. Table 3.5 shows body sizing parameters have been used. Elements start to grow with 0.01 element size in the circular and rectangular zones then it continues to grow from the border line of the influence body with 50 mm to the boundary of the domain to be 250 mm maximum size as it is shown in Figure 3.5.

Table 3.5 Body sizing parameters

Scoping method	Geometry selection
Geometry	1 body
Type	Body of influence
Body of influence	2 bodies
Element size	$1 \cdot 10^{-2}$ m
Growth rate	Default

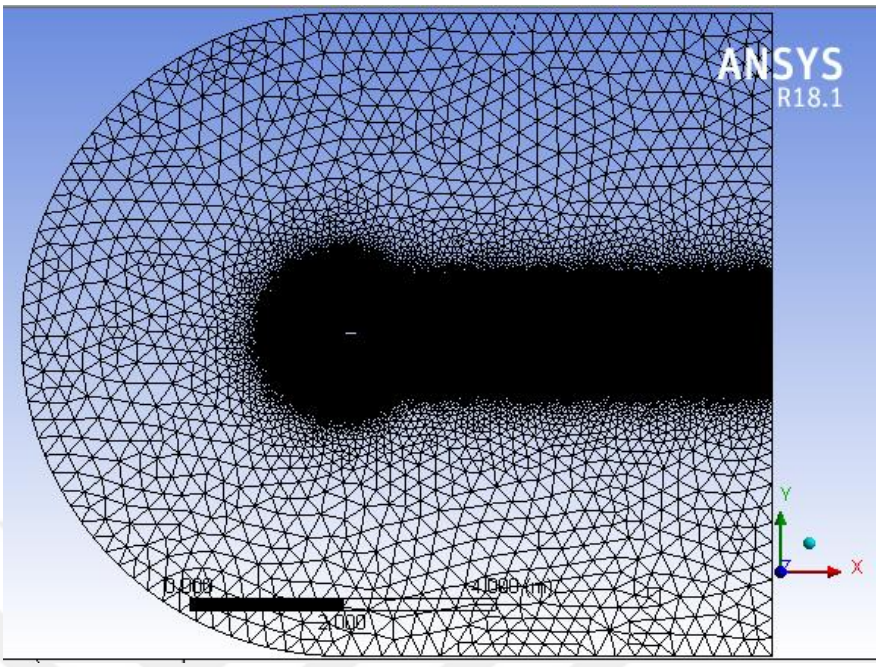


Figure 3.5 Elements growing gradually in body sizing

3.2.2.4 Mesh Quality

The quality of mesh plays an important role in both the accuracy of the results and the convergence of the solution, so in order to capture the flow physics correctly and for solution to be grid independent some criteria should be ensured. Low orthogonal quality or high skewness values are not recommended. Up to 0.98 skewness value ANSYS can run the simulation but it takes a long time to reach the convergence. In ANSYS equations solvers assume that cells are relatively equilateral or equiangular as shown in Figure 3.6. Mesh skewness was checked in this study, maximum skewness value is measured approximately 0.88 which is acceptable according to the skewness mesh metrics spectrum in Figure 3.7 [23].

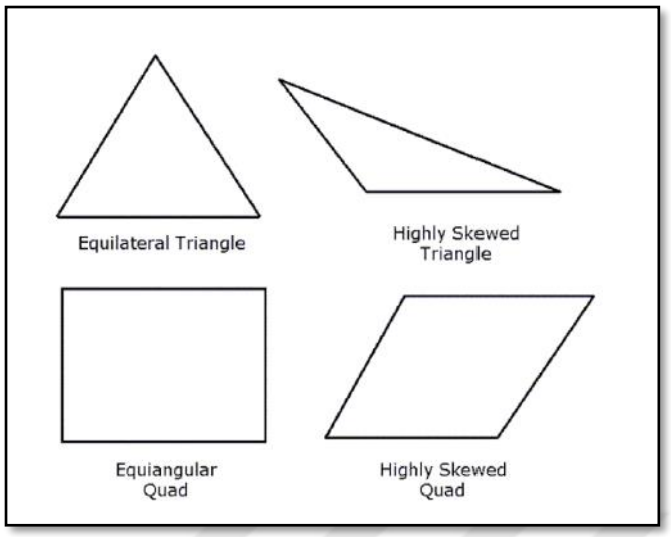


Figure 3.6 Skewness [22]

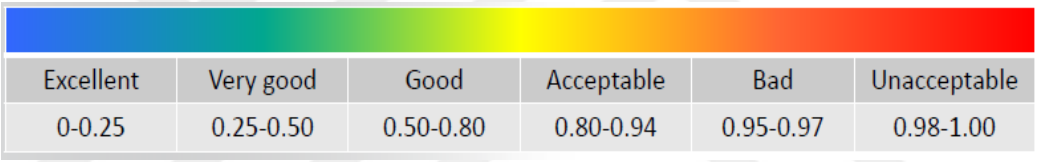
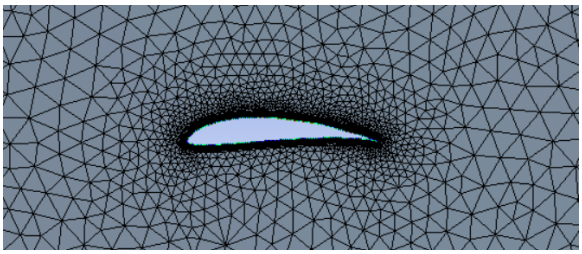


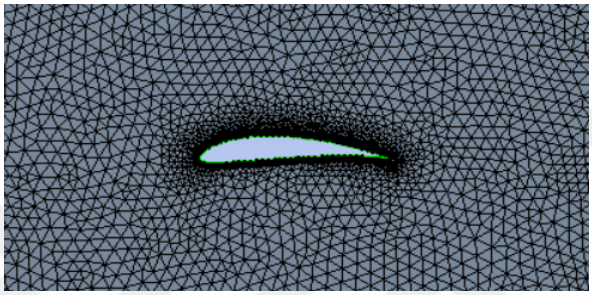
Figure 3.7 Skewness mesh metrics spectrum [23]

3.2.2.5 Grid Independence Study

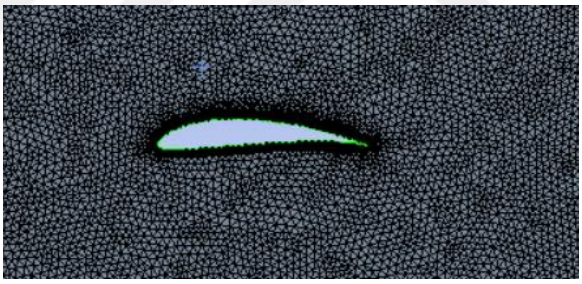
The grid independence study was performed changing the number of elements in the body of influence region as shown in Figure 3.8. Four different sizing were performed in the central zone around the airfoil and the zone behind the airfoil considering element size in the body of influence 0.04, 0.02, 0.01, 0.005 m, respectively. The other mesh settings were not modified while making mesh improvement operations.



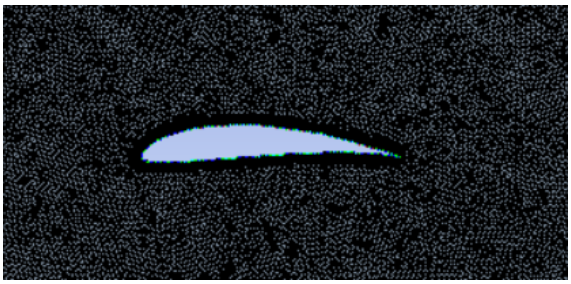
a) Course mesh-1 (24070 elements)



b) Course mesh-2 (66459 elements)



c) Middle mesh (229000 elements)



d) Fine mesh (855773 elements)

Figure 3.8 Different mesh sizes from course to fine

For mesh dependence study the airfoil drag coefficient C_d was set as the gauge. The 0.01 m element size mesh finally gave an accurate result. The element size was decreased, until further decreasing in the size of element caused no considerable difference in the C_d values as shown in Table 3.6 and Figure 3.9. After running the simulations, middle mesh was chosen for all airfoil simulations to keep short simulation time.

Table 3.6 Mesh refinement values

Mesh Refinement				
	Course-1	Course-2	Middle	Fine
Element Number	24070	66459	229000	855773
Element size	0.04m	0.02m	0.01m	0.005m
C_d value	0.020447	0.01869	0.017505	0.017192

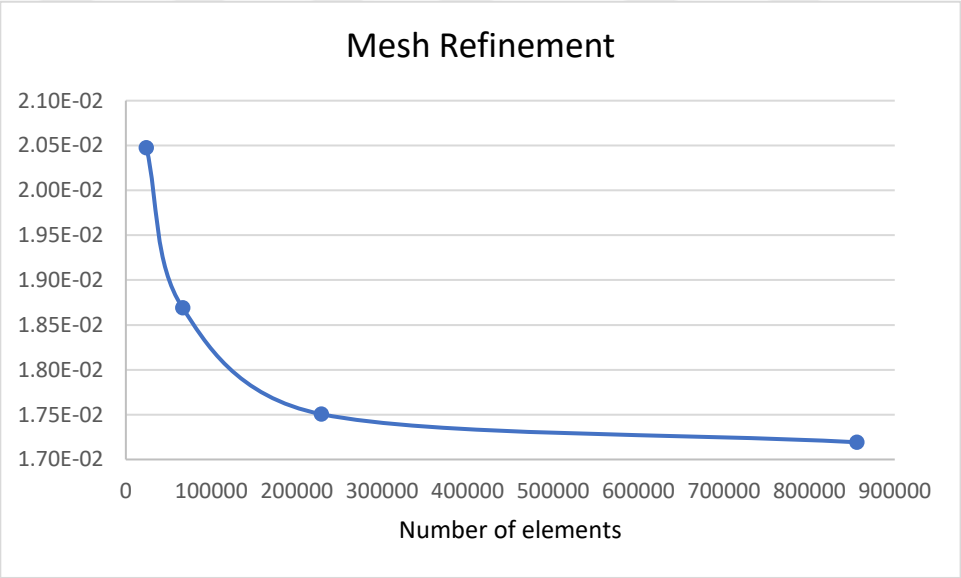


Figure 3.9 Mesh convergence curve

3.2.3 Numerical Setup

3.2.3.1 Fluent Launcher

Numerical calculations have been carried out with the help of two-dimensional (2D) simulation. In case the geometry is very thin in one direction and very long in the other direction also in case there are small cell sizes ranging to very large cell sizes in a single mesh double precision option was selected to capture the geometry and different cells in the domain. This will go down to 16 decimal places and obviously take nearly two times the memory and around 50% more solving time [24]. For single core CPU serial processing option is available. The Fluent launcher settings are presented in Table3.7.

Table 3.7 Fluent launcher settings

Dimension	2D
Options	Double precision
Processing option	Serial

3.2.3.2 General Settings

The mesh was checked for the minimum volume to make sure that even if it is very small it has a positive value. As the flow is incompressible so the density will be constant and Mach number is less than one. In this case a pressure-based solver has been selected [25]. For velocity formulation, it has been kept as absolute (default) as there is no rotating part in the study [24]. For time option the transient simulation is used because the simulations are in low Reynolds number and it has been intended to cover laminar separation phenomena which are rather over-time phenomenon [26]. Gravity has not been used because it does not affect the results in any significant way for horizontal flows, it can be activated for vertical flows or multi-phase droplets. Table 3.8 represents the solver general settings.

Table 3.8 Solver general settings

Type	Pressure-based
Velocity formulation	Absolute
Time	Transient
Gravity	Uncheck

3.2.3.3 Models

For low Reynolds simulations to capture the flow physics and predict more accurate results it is recommended to use Transition (γ-Reθ) Shear Stress Transport SST turbulence model which is advanced for transition flows. It is one of three Reynolds-averaged Navier–Stokes (RANS) turbulence models that allows for prediction of transition from laminar to turbulent. It is a combination of SST K-ω additionally coupled with intermittency γ and transition onset Reynolds number. It requires high mesh resolution near walls (y+ = 1) and it has been recommended for boundary layer transition only. Four transport equations are solved [27]. The Equation 3.7 for intermittency and Equation 3.8 for transition momentum thickness Reynolds number are given as follows [25]:

$$\frac{\partial(\rho\,\gamma)}{\partial t} + \frac{\partial \rho U_j \gamma}{\partial x_j} = P_x\gamma 1 - E_{\gamma 1} + P_{\gamma 2} - E_{\gamma 2} + \frac{\partial}{\partial x_j}\left[\left(\mu + \frac{\mu_t}{\sigma_\gamma}\right)\frac{\partial \gamma}{\partial x_j}\right] \quad \textbf{(3.7)}$$

$$\frac{\partial(\rho\,R\overline{e_{\theta t}})}{\partial t} + \frac{\partial(\rho U_j\,R\overline{e_{\theta t}})}{\partial x_j} = P_{\theta t} + \frac{\partial}{\partial x_j}\left[\sigma_{\theta t}(\mu + \mu_t)\,\frac{\partial R\overline{e_{\theta t}}}{\partial x_j}\right] \quad \textbf{(3.8)}$$

The coupling of transition model with SST K-ω is performed by modifying the K-equation in Equation 3.9[25].

$$\frac{\partial}{\partial t}(\rho\,k) + \frac{\partial}{\partial x_j}(\rho k u_i) = \frac{\partial}{\partial x_j}\left(\Gamma_k\,\frac{\partial k}{\partial x_j}\right) + G_k^* - Y_k^* + S_k \quad \textbf{(3.9)}$$

$$G_k^* = \gamma_{eff}\bar{G}_k$$

$$Y_k^* = \min\left(\max\left(\gamma_{eff}, 0.1\right), 1.0\right)Y_k$$

Curvature correction option has been selected to fairly capture eddies around the curvature of the airfoil. While the other options and the model constants have been remained as a program controlled (default) [25]. Viscous model settings are shown in Table 3.9.

Table 3.9 Viscous model settings

Model	Transition SST (4 eqs)
Transition SST options	Default
Options	Curvature correction
Model constants	Default
User-defined transition correlations	None

3.2.3.4 Materials and Operating Conditions

Table 3.10 represents fluid parameters of the air in the simulation. The material was chosen as a fluid type (air). Density and dynamic viscosity values of the air were entered for 600 meters altitude from U.S. standard atmosphere air properties table (ρ =1.1572 kg/m^3 and μ = 1.7704 x 10^{-5} kg/ (m·s)) [28]. To reduce round-off errors by making the solver work with smaller 'gauge' pressures for the boundary conditions, for incompressible flows the operating pressure is specified typically to atmospheric thus, operation cell zone conditions has been set to 95590 Pa.

Table 3.10 Fluid parameters

Fluent fluid materials	Air
Density	1.1572 kg/m^3
Dynamic viscosity	$1.7704.10^{-5}$ kg/ (m · s)
Fluent solid materials	Default
Operating pressure	95590 Pa

3.2.3.5 Boundary Conditions

The inlet has been defined as velocity inlet with 13 m/s speed. For different angles of attack the component of the velocity has been defined in terms of X-component of flow direction, and Y-component of flow direction, these values are specified by cos (α) and sin (α), respectively. Outlet was defined as pressure outlet. For external flows, turbulent viscosity ratio ranges from 1 to 10 and turbulence intensities are between1%-5%. Turbulence intensity and viscosity ratio have been remained in default values [29]. Table 3.11 shows the boundary conditions of the simulation.

Table 3.11 Boundary conditions

Inlet and outlet parameters	
Velocity magnitude	13 m/s
X-component of flow direction	cos (α)
Y-component of flow direction	sin (α)
Gauge pressure	0 Pa
Turbulent intensity	Default
Turbulent viscosity ratio	Default

3.2.3.6 Dynamic Mesh

As long as there is no moving part in the model so there will not be required to remesh the model during the calculation thus the dynamic mesh option has not been used.

3.2.3.7 Reference Values

Reference values are represented in Table 3.12. These are not used to compute the flow solution, but they are used to report coefficients such as the lift, drag, and moment coefficients and in order to non-dimensionalize the forces and moments acting on the airfoil. The free-stream has been used as a reference condition and the reference values for velocity, density, temperature, etc. have been computed from inlet velocity.

Table 3.12 Reference values

Density	1.1572 kg/m^3
Depth	0.280 m
Enthalpy	0 J/kg
Length	0.280 m
Pressure	0 Pa
Temperature	288.16 K
Velocity	13 m/s
Dynamic viscosity	$1.7704 \cdot 10^{-5}$ kg/ (m · s)
Ratio of specific heats	1.4

The reference value of length, depth, and area are not updated from the velocity conditions, but they have been set to represent a chord length of 0.280 m. Thus, the areas of the different airfoils are presented in Table 3.13.

Table 3.13 Areas of airfoils

HS520	0.054393 m^2
MH114	0.085295 m^2
MH45	0.061025 m^2
MH60	0.062942 m^2
SA7035	0.060283 m^2
SA7038	0.060386 m^2
SD7090	0.066675 m^2

3.2.3.8 Solution Method

Pressure velocity coupled solver has been used to reach the convergence of the solution much faster than the simple solver and in less iterations. As the program has been recommended, the least squares cell based gradient method has been set. In order to accurately predict drag, the default first order schemes are not sufficient; so, special discretization for pressure, momentum, turbulent kinetic energy, specific dissipation

rate, intermittency, and momentum thickness Re number options have been set to the second order [30]. Solution method settings are represented in Table 3.14.

Table 3.14 Solution methods

Pressure-velocity coupling scheme	Coupled
Gradient	Least squares cell based
Pressure	Second order
Momentum	Second order
Turbulent kinetic energy	Second order upwind
Specific dissipation rate	Second order upwind
Intermittency	Second order upwind
Momentum thickness Re number	Second order upwind
Transient Formulation	Second order implicit

3.2.3.9 Solution Controls

The parameters of solution controls are shown in Table 3.15. The under-relaxation factors have a big effect on the accuracy of the solution and the results, so they have been kept at their default values. Courant Number has been kept as a default. [31].

Table 3.15 Solution controls

Flow courant number	200
Explicit relaxation factors	Default
Under-relaxation factors	Default

3.2.3.10 Solution Monitors

The convergence of the solution has monitored by plotting residuals with setting the criteria of all the residuals to 0.001 for engineering solution that considered accurate enough that the calculation can stop when the residuals reach these pre-defined convergence criteria. The drag coefficient and the lift coefficient have been monitored also on the bottom-airfoil and top-airfoil wall zones. They were observed until C_d and

C_l converged. The force vector values for drag coefficient are x=cos (α) and y=sin (α) while for lift coefficient they are x=-sin (α) and y=cos (α).

3.2.3.11 Solution Initialization

Fluent has to be provided some initial values to start iteration. The hybrid solution initialization is recommended because it improves the convergence robustness for many cases [30].

3.2.3.12 Run Calculation

Implementing transient calculations are in some ways similar to implementing steady state calculations, but there are additional considerations like selecting the transient time step size. Time step has been used for unsteady simulations has to achieve a very simple condition: for the given time step, a fluid particle is not allowed to go through more than one cell. This can affect accuracy of the results and solution's convergence. The time step can be calculated using the formula 3.10 [32].

$$\text{Courant number} = \frac{Characteristic\ flow\ velocity * \Delta t}{Typical\ cell\ Size} \quad \textbf{(3.10)}$$

Transient analysis was carried out for by setting the typical cell size based on the first layer wall distance and courant number=200 by applying the formula 3.7 the time step has to be taken as 0.0004s. But for purpose of saving computing time in some cases of angle of attack the transient simulations have been carried out with time step= 0.002s. The residuals have been monitored and they reduced by around three orders of magnitude within one-time step as shown in Figure 3.10, so the criteria have been met and this will ensure accurate resolution of transient behavior [32].

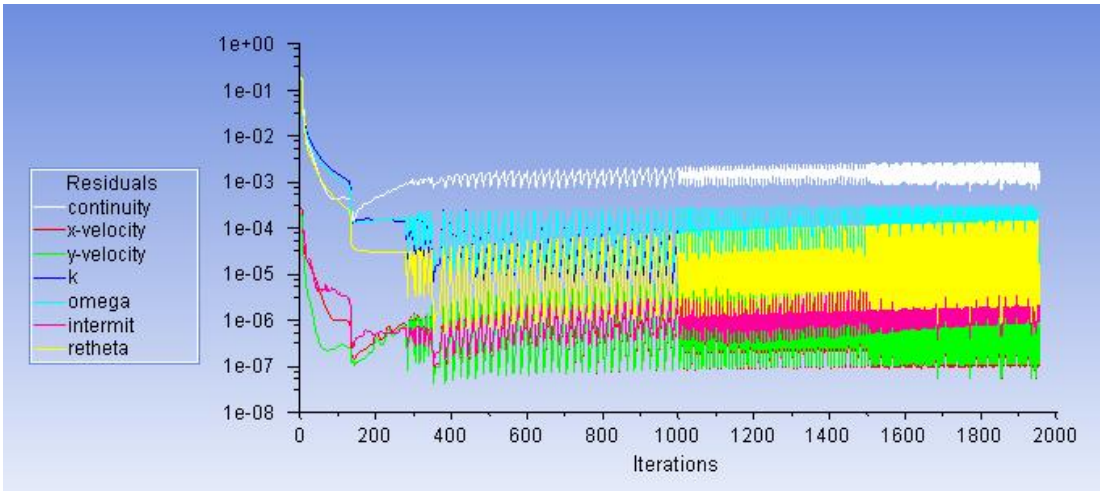


Figure 3.10 Scaled residuals history of transient solver is converged

CHAPTER 4

SIMULATION RESULTS AND DISCUSSION

The goal of this study is to investigate the performance and aerodynamic characteristics of airfoils for a range of angle of attack between -3 and 15 degrees with a 3-degree interval.

4.1 Airfoil Selection Criteria

As the UAV has been designed for aero photography and surveillance applications the stalling speed needs to be at low levels to ensure high quality photos and videos so the coefficient of lift at stalling speed is an important criterion that has been considered in the selection process. The lift coefficient at flight is a significant factor that affects the lifting force. In order to enhance the endurance of the design C_l/C_d ratio has been taken in account during the choosing process. Gentle variation in the lift curve in the stall region has been preferred which represents the stalling characteristics. Both wing airfoil ideal lift coefficient C_{l_i} and wing airfoil lift coefficient at stall speed $C_{l_{stall}}$have been calculated from the approximate Equation 4.1 by calculating the aircraft ideal cruise lift coefficient C_{L_c} in Formula 4.2 and wing cruise lift coefficient $C_{L_{c_w}}$ using the approximate relationship 4.3 [33].

$$C_{l_i} = \frac{C_{L_{c_w}}}{0.9} \quad \textbf{(4.1)}$$

Where, $C_{L_{c_w}}$: Wing cruise lift coefficient

$$C_{L_c} = \frac{2\,W}{\rho\,U^2\,S} \quad \textbf{(4.2)}$$

Where,

C_{L_c}: Aircraft ideal cruise lift coefficient.

W: Weight of UAV (kg).

ρ: Air density at cruising altitude (m).

U: Aircraft cruise speed (m/s).

S: Wing planform area (m^2).

$$C_{L_{c_w}} = \frac{C_{L_c}}{0.95} \quad \textbf{(4.3)}$$

Submitting in the previous equations the wing airfoil ideal lift coefficient for the designed small unmanned aerial vehicle $C_{l_i} = 0.2$ and the wing airfoil lift coefficient at stall speed $C_{l_{stall}} = 0.5$.

Since not all design requirements have the same importance, the criteria have been compromised using Weighted Scoring Method as it is represented in the Table 4.1 [12].

Table 4.1 Criteria for flying wing airfoil selection.

Criterion	C_l	C_l/C_d	**Total**
Score of factors	60	40	100
HS520	0.12279	9.04	3.68974
MH114	0.726255	40.79	16.75193
MH45	0.12517	10.2	4.155102
MH60	0.12975	11.2	5.2585
SA7035	0.33817	28.4	11.5629
SA7038	0.42668	35.1	14.29601
SD7090	0.25469	24.6	9.992814

According to Table 4.1 MH114 wing airfoil gained the higher score among all the airfoils and satisfied the design requirements.

4.2 Lift Coefficient, C_l

Figure 4.1 shows the graphs of coefficient of lift $C_l$versus angle of attack for all the airfoils. As the angle of attack increased, the coefficient of lift increased in all airfoils until α =12 degree. Except for MH45 and SD7090 airfoils, the lift coefficient starts decreasing after α =12 degree in all the other airfoils so the critical α of these airfoils is between 12-15 degrees and by increasing α the airfoils were under stall condition. The lift coefficient of MH45 and SD7090 kept increasing after α =12 degree. However, lift coefficient curve of MH 114 airfoil shows the highest values of C_l in all angles of attacks among all the other airfoils' lift coefficient curves.

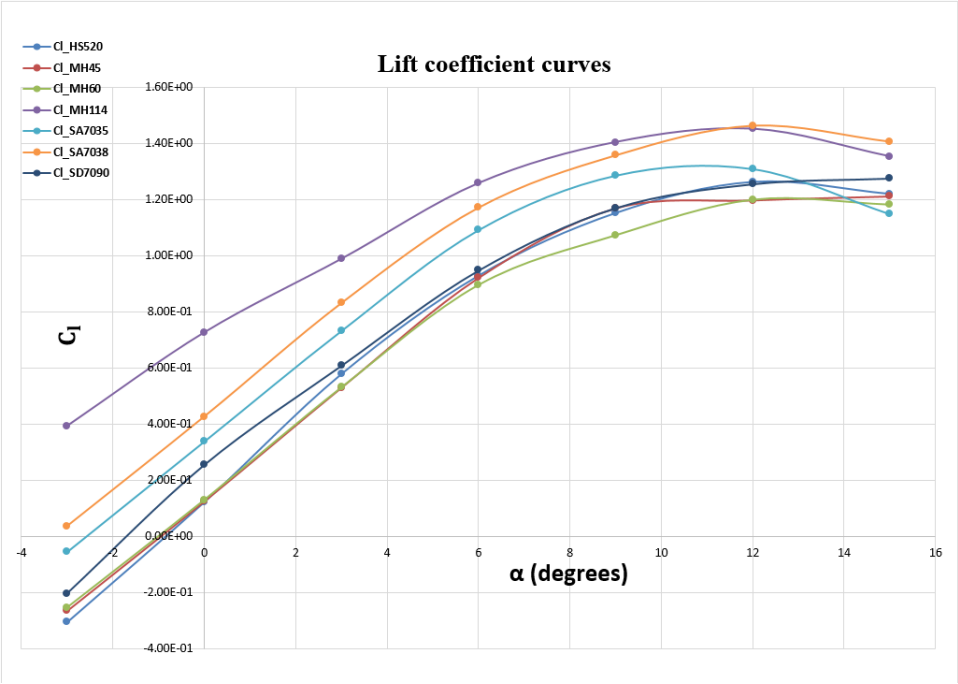


Figure 4.1 C_l- α curves of the airfoils

4.3 Drag Coefficient, C_d

Figure 4.2 shows the graphs of coefficient of drag versus angle of attack for all the airfoils. The drag coefficients of all the airfoils were slightly increasing as angle of attack increased until the angle of attack around 10 degree after that α the value of C_d start increasing dramatically. It is noticeable that the coefficient of drag of MH114 airfoil has different behavior comparing to the other airfoils after α =10 degree. It did not show very big varying in the increasing of C_d so in general this airfoil produces less drag than the others. Before the α=10°, C_d- α curves for all airfoils follow analogous directions of the results which are completely overlapping each other, however the drag experienced by the MH114 airfoil is marginally lower than the other's drag.

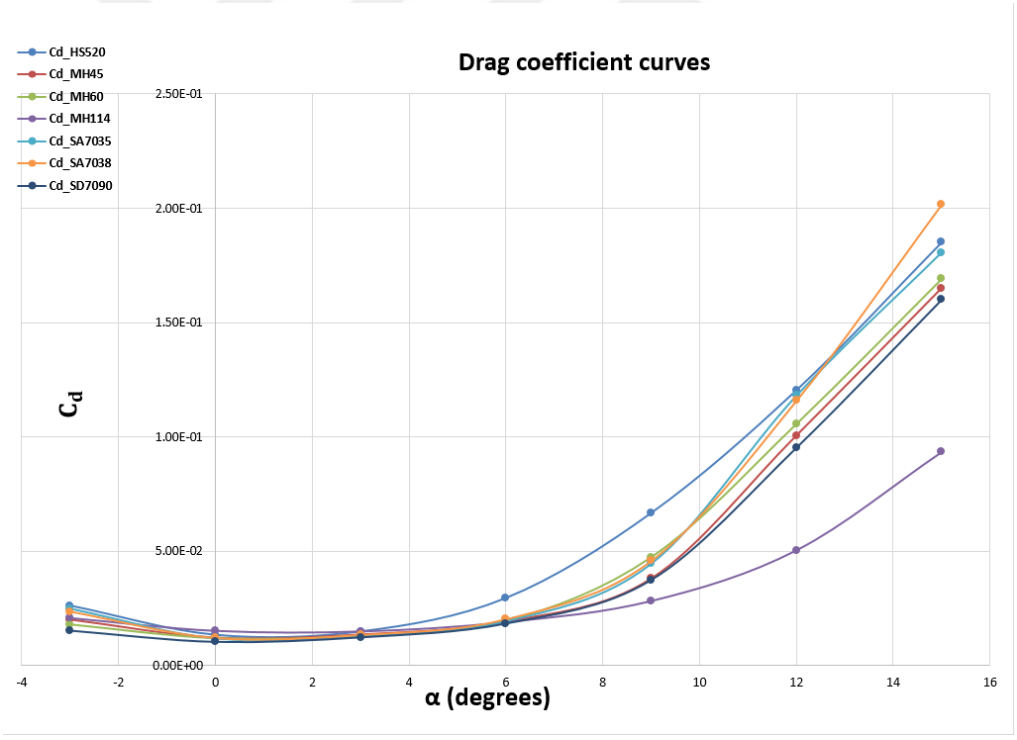


Figure 4.2 C_d- α curves of the airfoils

4.4 Lift-to-Drag Ratios, C_l/C_d

As the selection process have been chosen for α =0° a lift-to-drag ratio C_l/C_d is calculated to compare various scenarios. The lift to drag ratio at α =0 degree of the airfoils is represented in Table 4.2.

Table 4.2 C_l/C_d for all the airfoils at α =0

Airfoil	C_l/C_d
HS520	9.04
MH114	40.79
MH45	10.2
MH60	11.2
SA7035	28.4
SA7038	35.1
SD7090	24.6

Aircraft which has an airfoil that provides the highest C_l value when C_d value is low, will be more efficient and could fly more time with less power consuming. According to the results of C_l/C_d , the MH114 airfoil profile get the highest value of C_l/C_d . The corresponding results are shown in Figure 4.3.

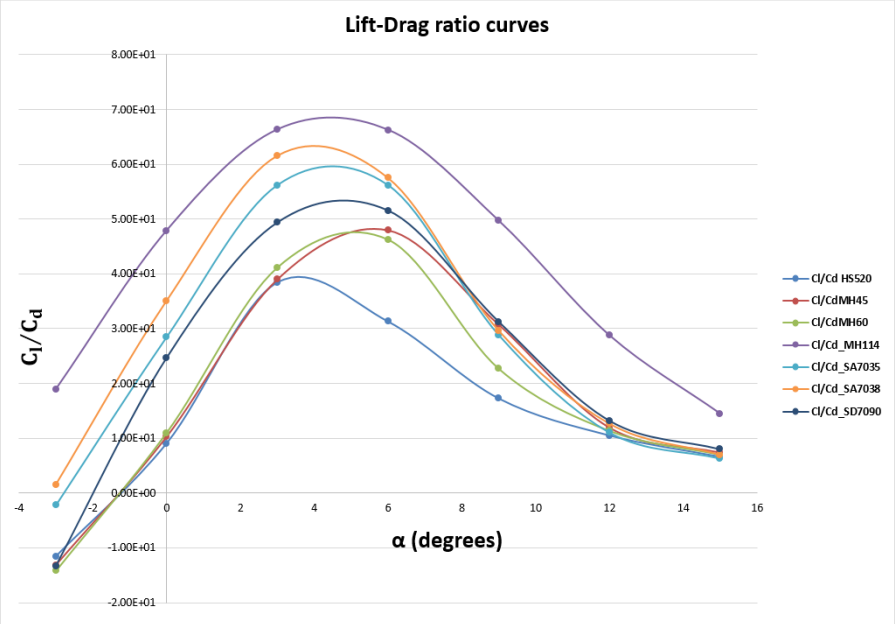


Figure 4.3 C_l/C_d- α curves of the airfoils

4.5 Flow Field Analysis for MH114

The intermittency contour, pressure contour, pressure coefficient distribution, velocity contour, velocity streamlines and turbulent kinetic energy distribution have been investigated to examine flow behavior around MH114 airfoil using post-processing of Fluent.

4.5.1 Contour of Intermittency

Figure 4.4 represents the intermittency contour for different angles of attack. Transition occurred in the region where the value of intermittency increased from 0 (laminar) to 1 (fully turbulent). The transition happened closer to the leading edge by increasing the angle of attack.

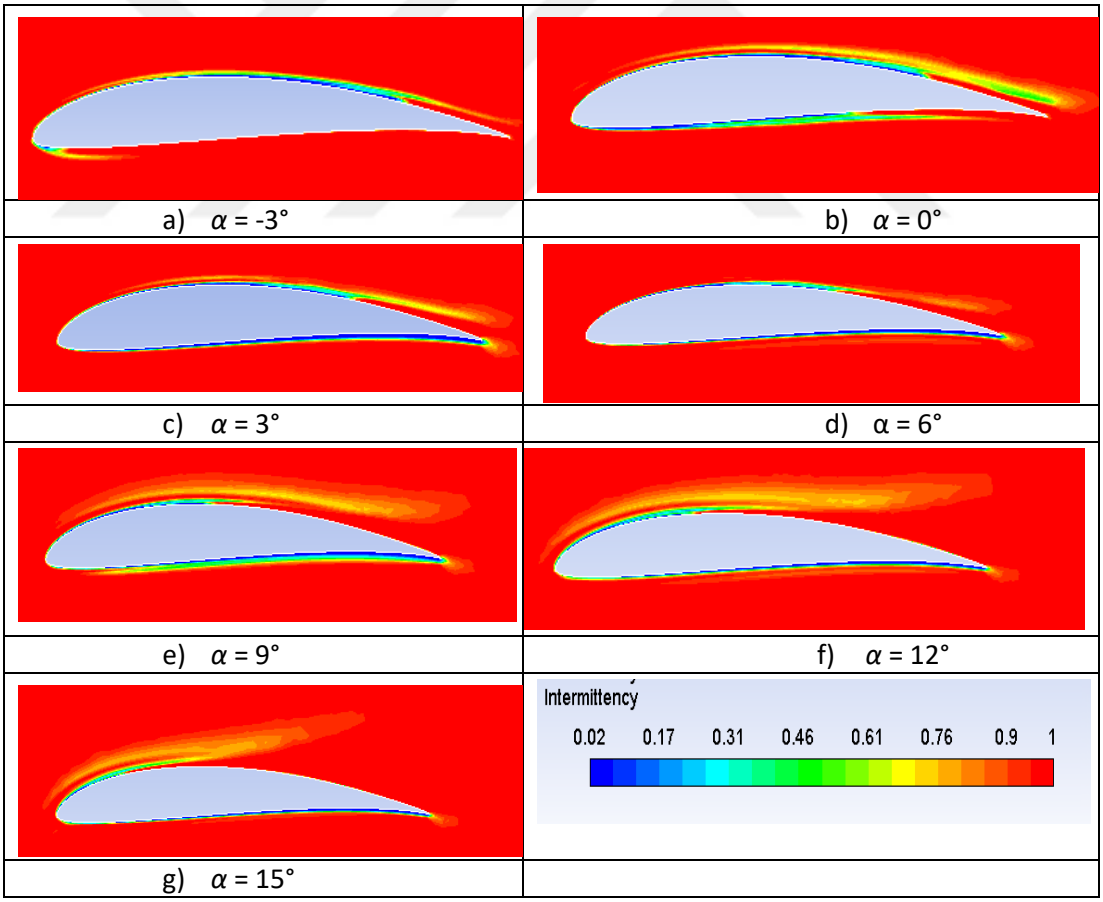


Figure 4.4 Contour of intermittency for different α (-3°, 0°, 3°, 6°, 9°, 12°, 15°) degrees

4.5.2 Contour of Pressure

Figure 4.5 shows the contour plot of pressure distribution across the airfoil for different angles of attack. In the spectrum, the colors towards the blue signify low pressure regions while the colors towards the red signify high pressure zones. From the pressure contours plot, on the upper surface of the airfoil low pressure region was noticed and high-pressure zone was under the airfoil. At the leading edge, it was also observed region of high pressure (stagnation point).

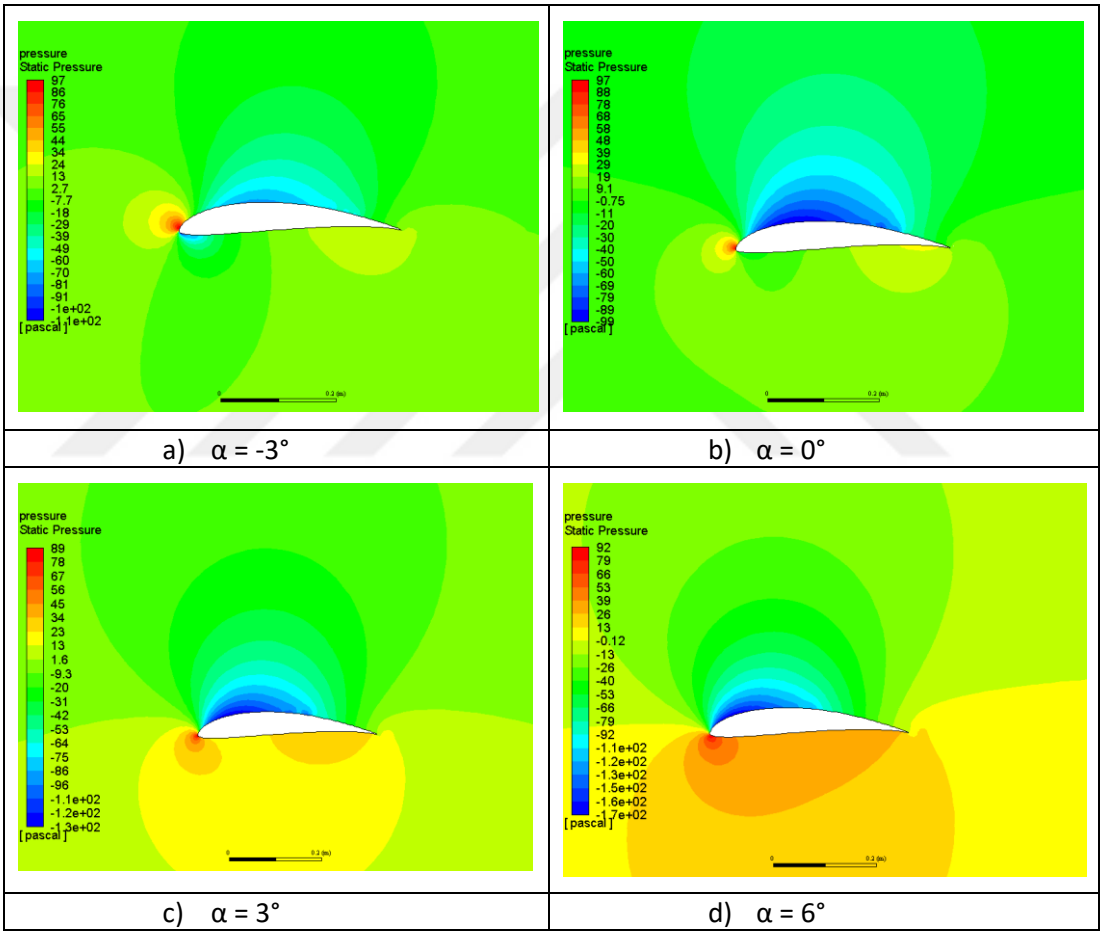


Figure 4.5 Contour of pressure for different α (-3°, 0°,3°, 6°, 9°, 12°, 15°) degrees

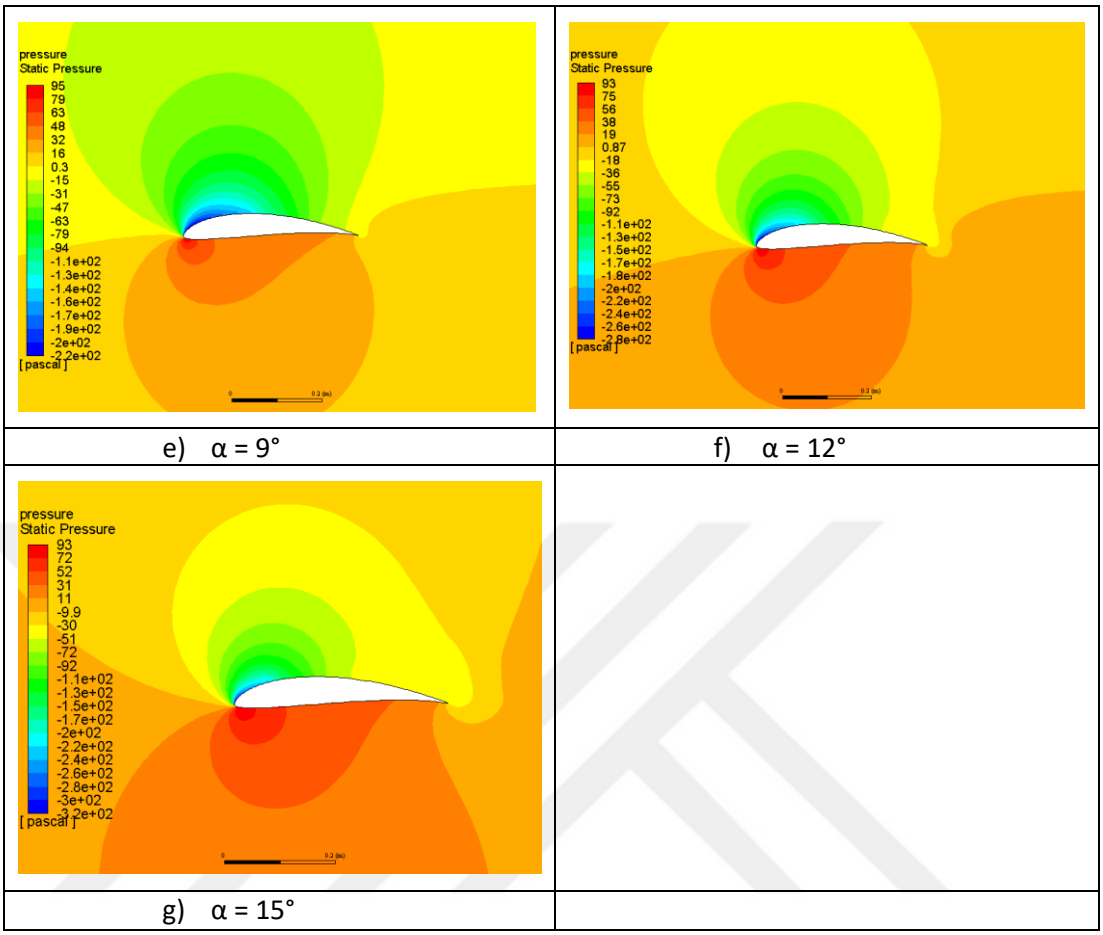


Figure 4.5 (continued) Contour of pressure for different *α* (-3°, 0°,3°, 6°, 9°, 12°, 15°) degrees

4.5.3 Coefficients of Pressure

Figure 4.6 represents the distribution of pressure coefficients for different angles of attack. On the lower surface the increase in the pressure is less than the decrease in it on the upper surface of the airfoil. When the angle of attack increased the high pressure on the lower surface remained constant while the negative pressure on the upper surface of the airfoil increased thus the difference in pressure between both surfaces increased which implied higher lift. The upper surface of an airfoil provides the greater portion of the lift as the angle of attack increased the position of the lowest pressure zone moved towards the leading edge. The most obvious decreasing of pressure on the top surface and the increasing of pressure on the bottom surface of the airfoil were over the front part of the airfoil.

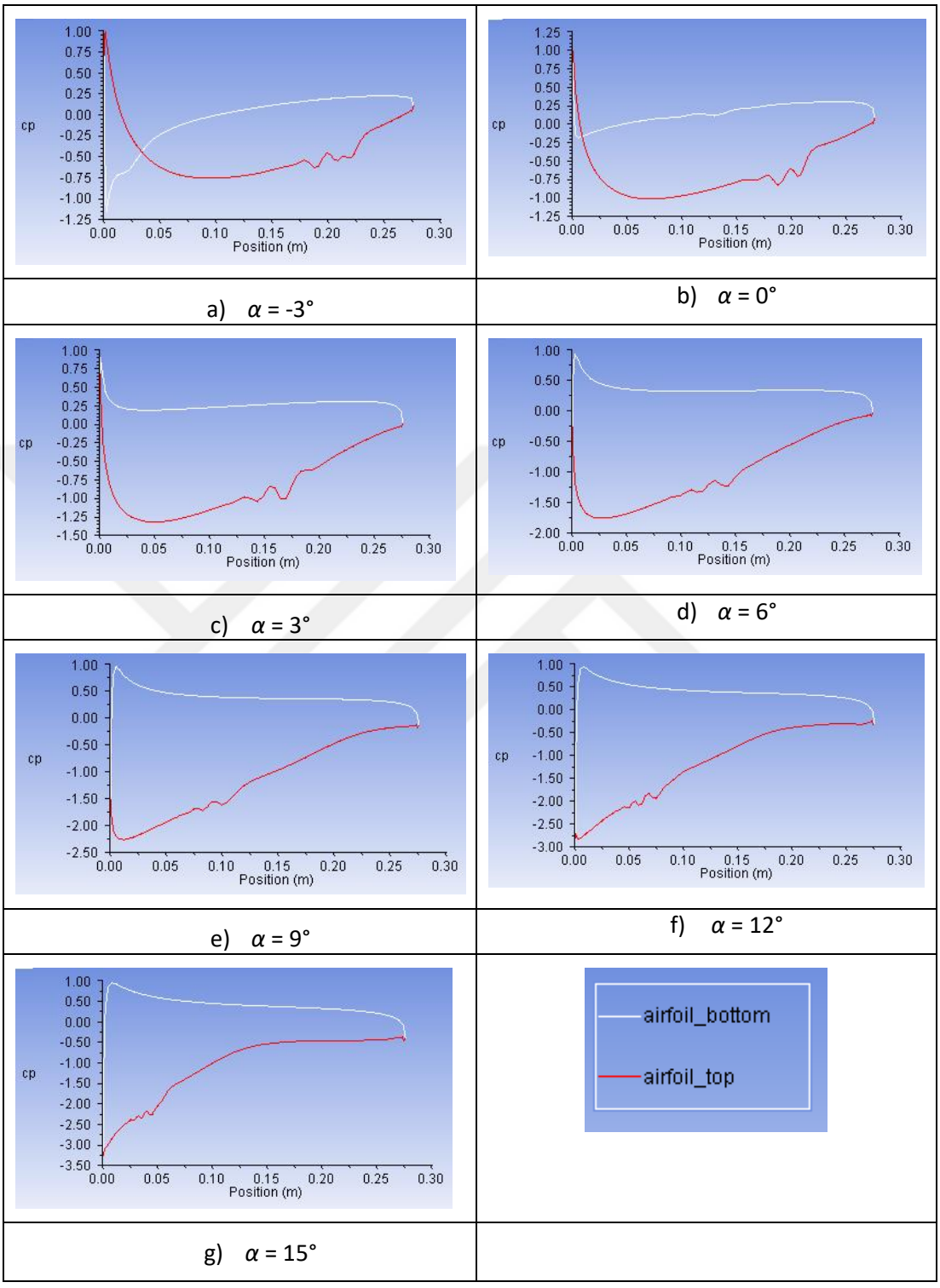
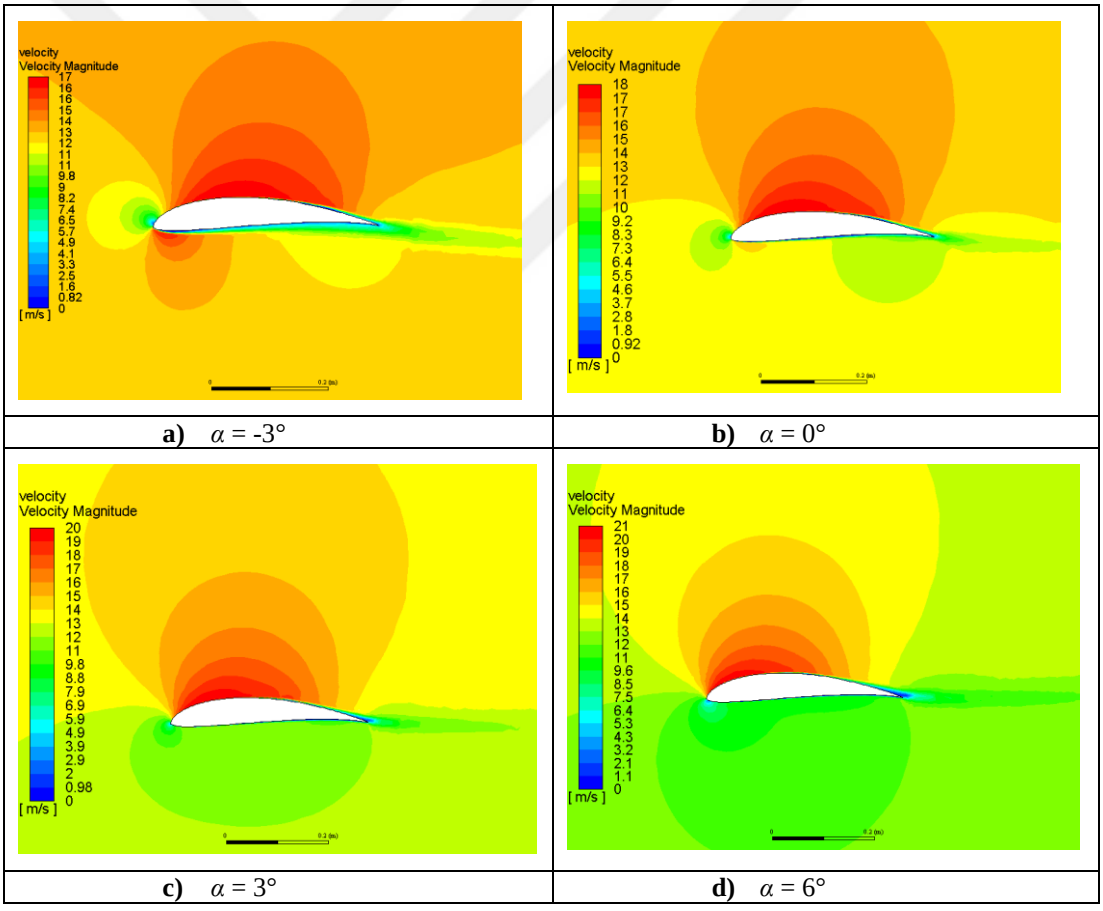


Figure 4.6 Pressure coefficient profiles for different α (-3°, 0°,3°, 6°, 9°, 12°, 15°) degrees

4.5.4 Contour of Velocity

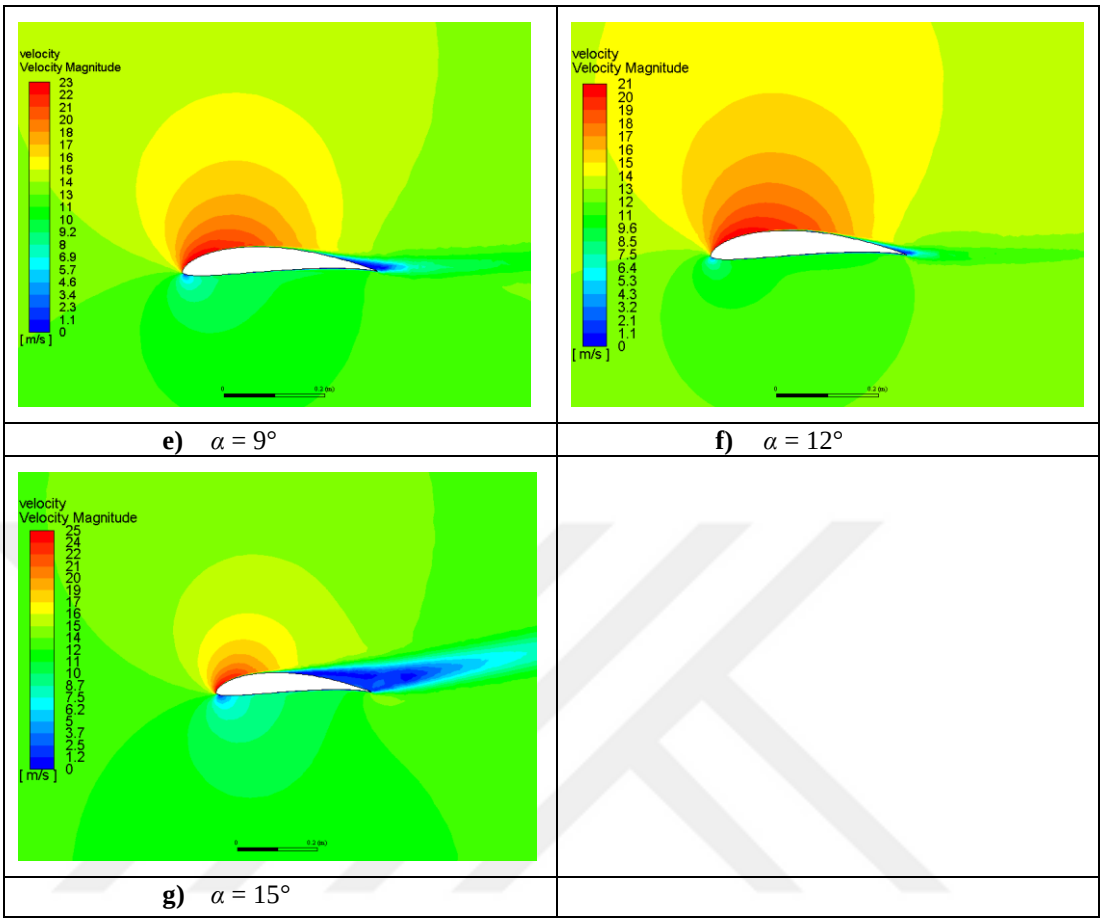
Figure 4.7 shows the contour plots of velocity distributions across the airfoil for different angles of attack. In the spectrum, the colors towards the blue end stand for low velocity, while the colors towards the red end stand for high velocity. The velocity in the upper surface was bigger than its value in the lower surface of the airfoil and by increasing the angle of attack the difference of velocity between surfaces increased. At the trailing edge the blue regions stand for very low velocity value which indicates flow separation in these areas at all angles of attack. However, the flow separation was small at α= 6º while it increased dramatically with the increasing of the angles of attack and this increment in the flow separation was due to formation of eddies.



a) α = -3° **b)** α = 0°

c) α = 3° **d)** α = 6°

Figure 4.7 Contour of velocity for different α (-3°, 0°,3°, 6°, 9°, 12°, 15°) degrees



e) α = 9° **f)** α = 12°

g) α = 15°

Figure 4.7 (continued) Contour of velocity for different α (-3°, 0°,3°, 6°, 9°, 12°, 15°) degrees

4.5.5 Streamlines of Velocity

4.5.5.1 The Region Near the Trailing Edge

Figure 4.8 shows velocity streamlines showing vortex development in the air on the upper surface of the airfoil near the leading edge for different angles of attack. The vortex created in the flow field of an airfoil depends on α. Below α = 6°, no vortices are noticed near the trailing edge of the airfoil. The trailing edge vortex was observed at α = 6°, at the trailing edge the separated flow on the upper surface formed vortices. One more vortex was observed covered the upper surface of the airfoil at the trailing edge it has started growing at α=9° then it can be seen more obvious from the streamline patterns of α = 12° which were clear at higher angles of attack and these vortices were keeping growing by increasing α. This proofed turbulence presence in that region. From the velocity streamline it was clearly observed that as the angle of

attack increased the flow separation point on the suction surface moved upstream towards the leading edge.

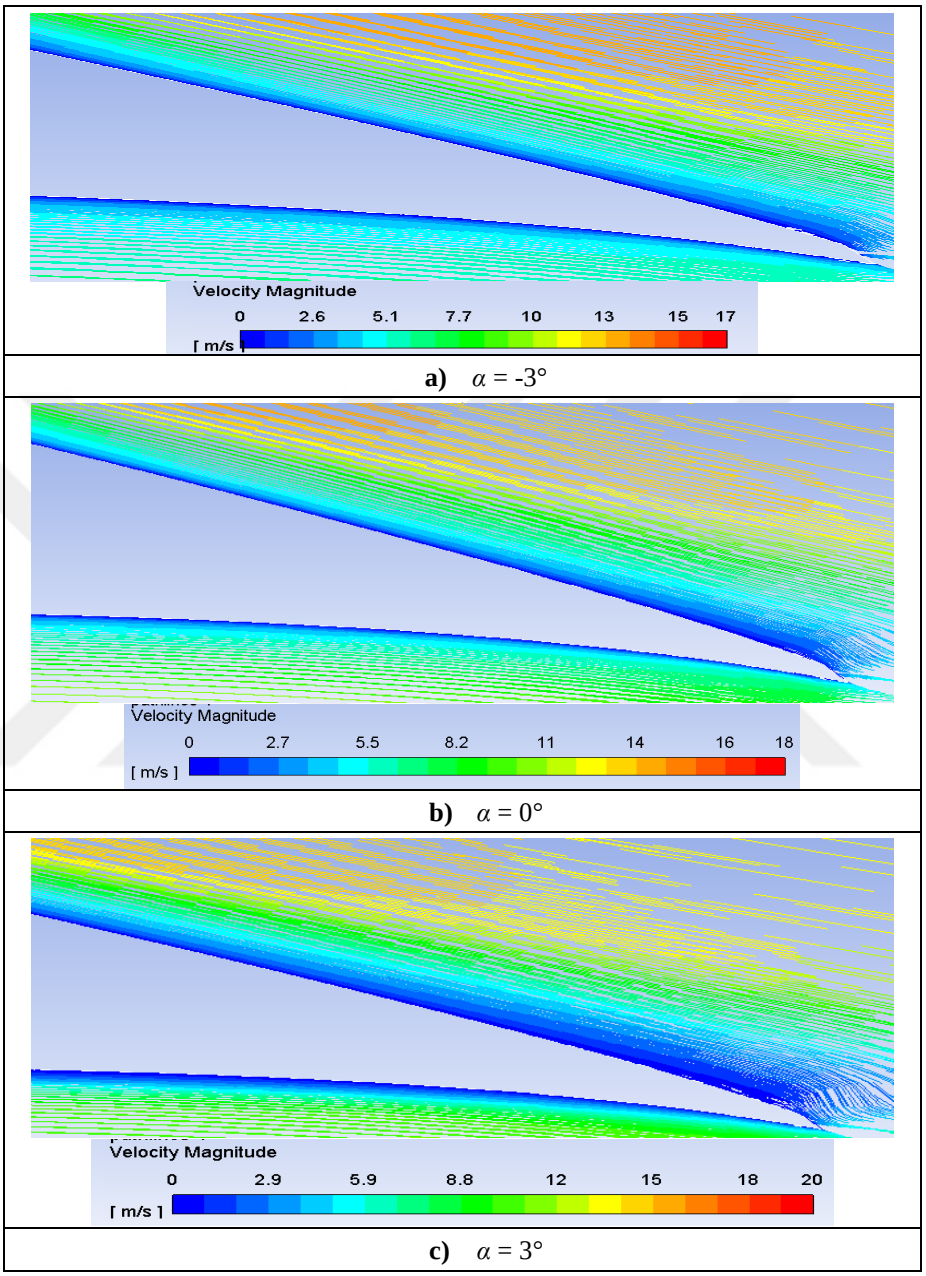
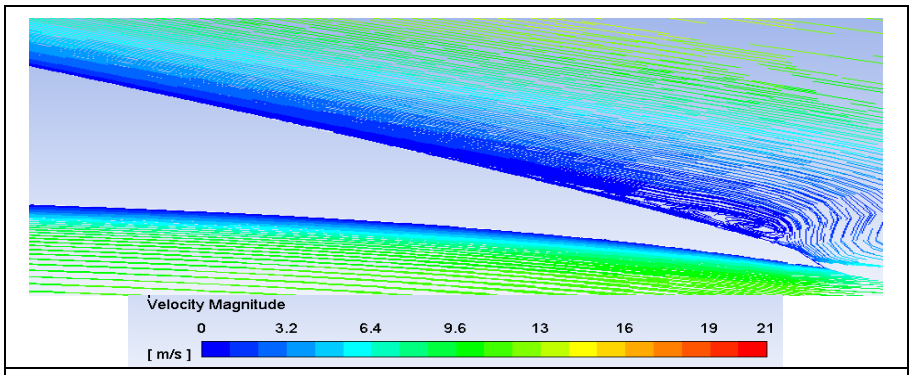
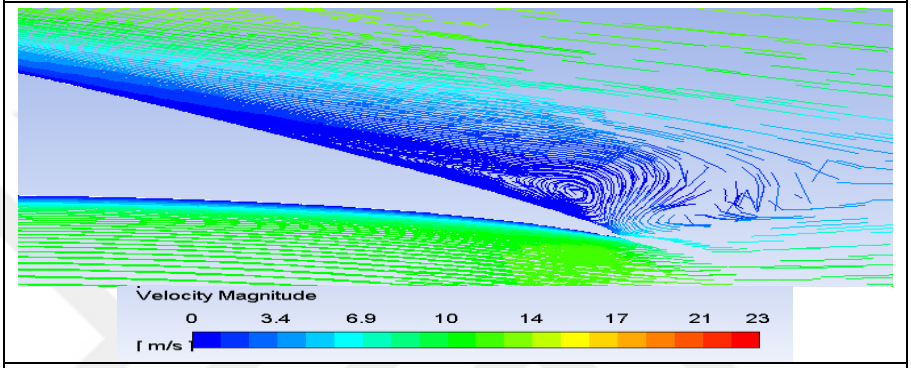


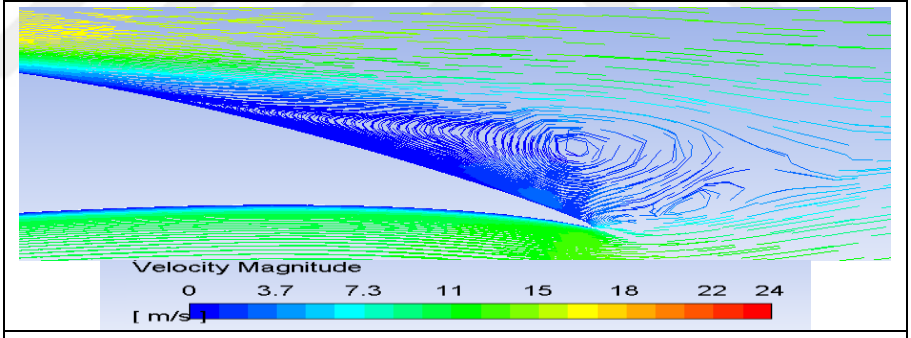
Figure 4.8 Velocity streamlines near the trailing edge at different α (-3°, 0°, 3°, 6°, 9°, 12°, 15°) degrees



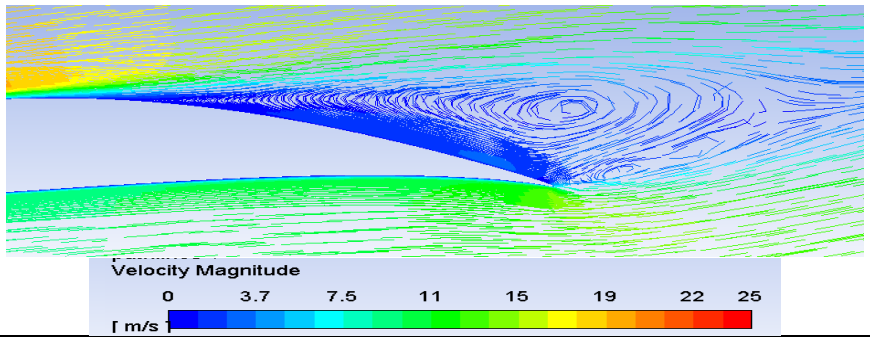
d) $\alpha = 6°$



e) $\alpha = 9°$



f) $\alpha = 12°$



g) $\alpha = 15°$

Figure 4.8 (continued) Velocity streamlines near the trailing edge at different α (-3°, 0°, 3°, 6°, 9°, 12°, 15°) degrees

4.5.5.2 The Laminar Separation Bubbles

The laminar separation bubbles on the suction surface of the airfoil represented by velocity streamline property for flow angles ranging from -3 to 15 are shown in Figure 4.9. The adverse pressure gradient was server enough that the laminar layer separated near the trailing edge of the suction surface of the airfoil at α=-3, forming three vortexes and transitioned to turbulence then reattached. As α increased, the bubbles moved towards the leading edge and their sizes reduced gradually.

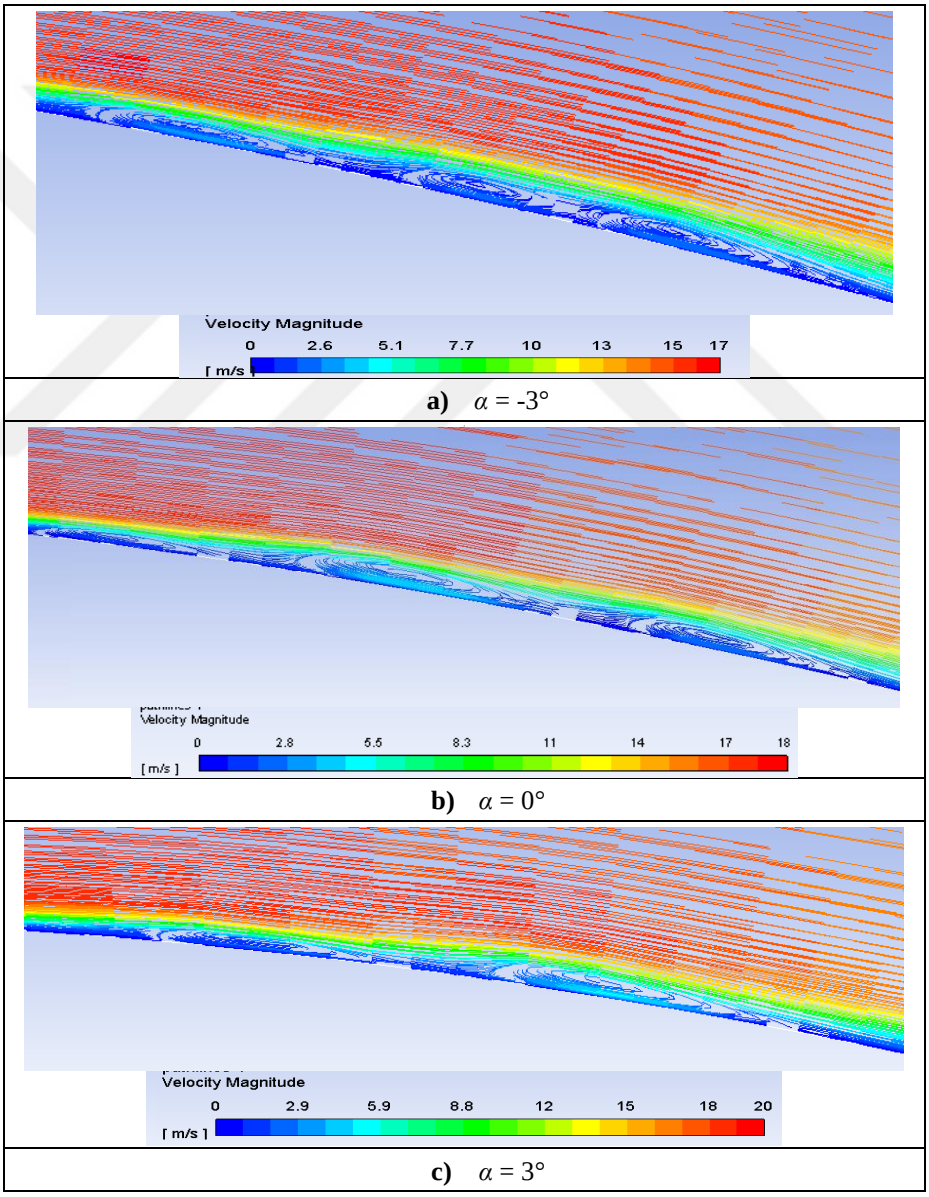
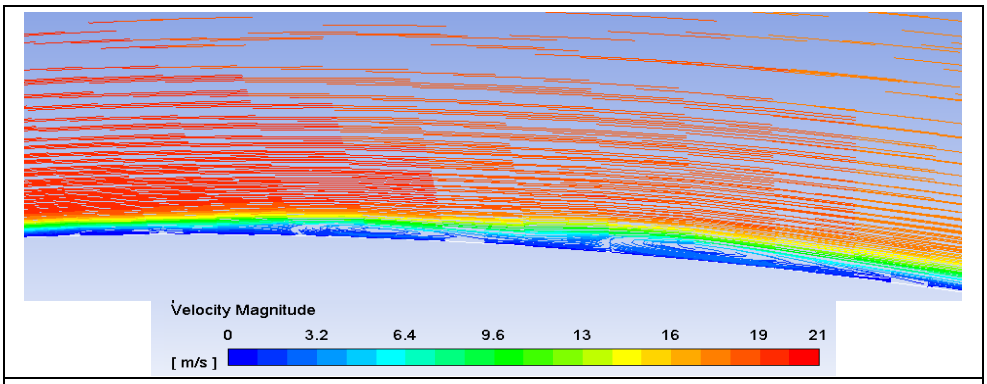
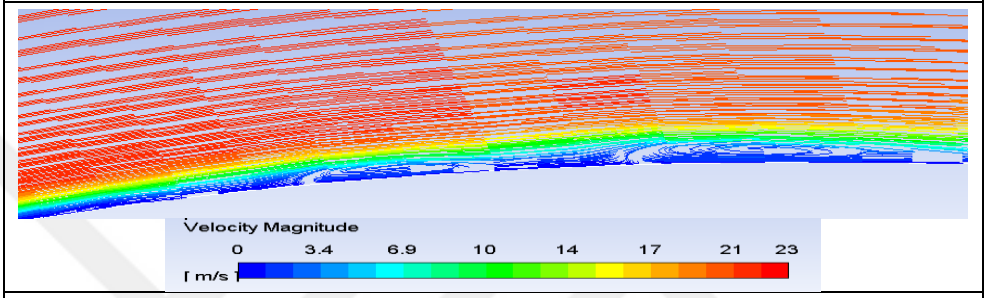


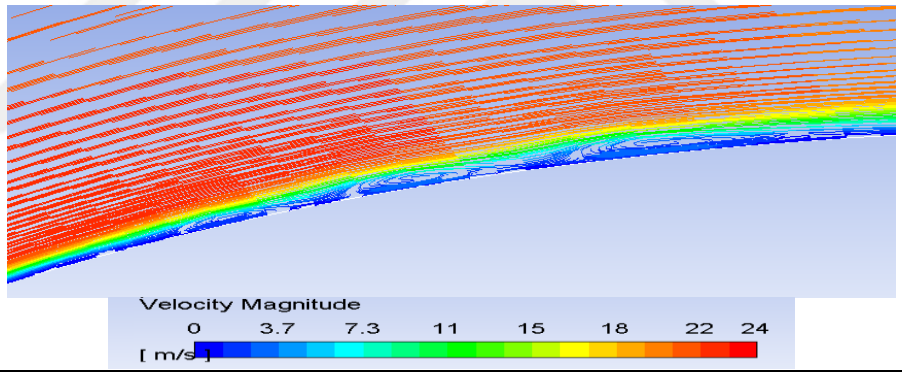
Figure 4.9 Velocity streamlines in the suction surface of the airfoil at different α (-3°, 0°, 3°, 6°, 9°, 12°, 15°) degrees



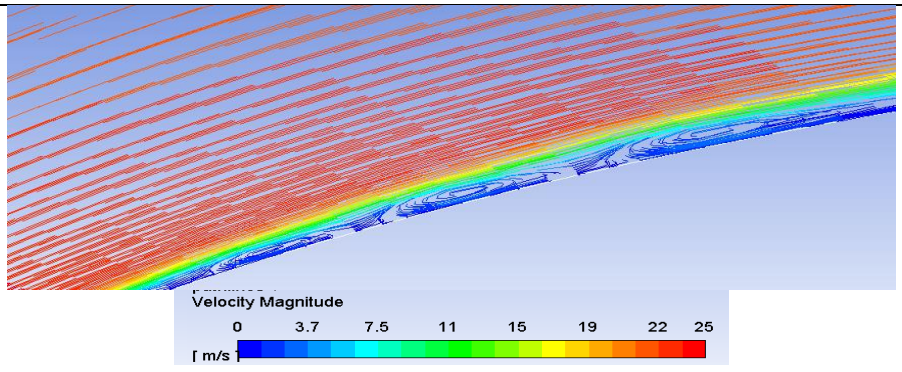
a) $\alpha = 6°$



b) $\alpha = 9°$



c) $\alpha = 12°$



d) $\alpha = 15°$

Figure 4.9 (continued) Velocity streamlines in the suction surface of the airfoil at different α (-3°, 0°, 3°, 6°, 9°, 12°, 15°) degrees

4.5.6 Turbulent Kinetic Energy Distribution

The distributions of turbulent kinetic energy (TKE) around the airfoil for angles ranging from -3º to 15º are shown in Figure 4.9. At α=-3° laminar boundary layer was predicted over the more than a half of the airfoil suction surface and had minimum TKE, while the pressure surface had higher TKE distribution. At α=0° the flow separation on the suction surface moved upstream towards the leading edge and flow separation point on the pressure surface moved downstream towards the trailing edge. Then, as the angle of attack increased the adverse pressure gradient became intense enough that the laminar boundary layer separated, transitioned to turbulence and reattached and the separation point kept moving closer and closer towards the leading edge and minimum TKE observed on the pressure surface of the airfoil. In addition, higher TKE distribution has been found in the separated flow zone near the trailing edge.

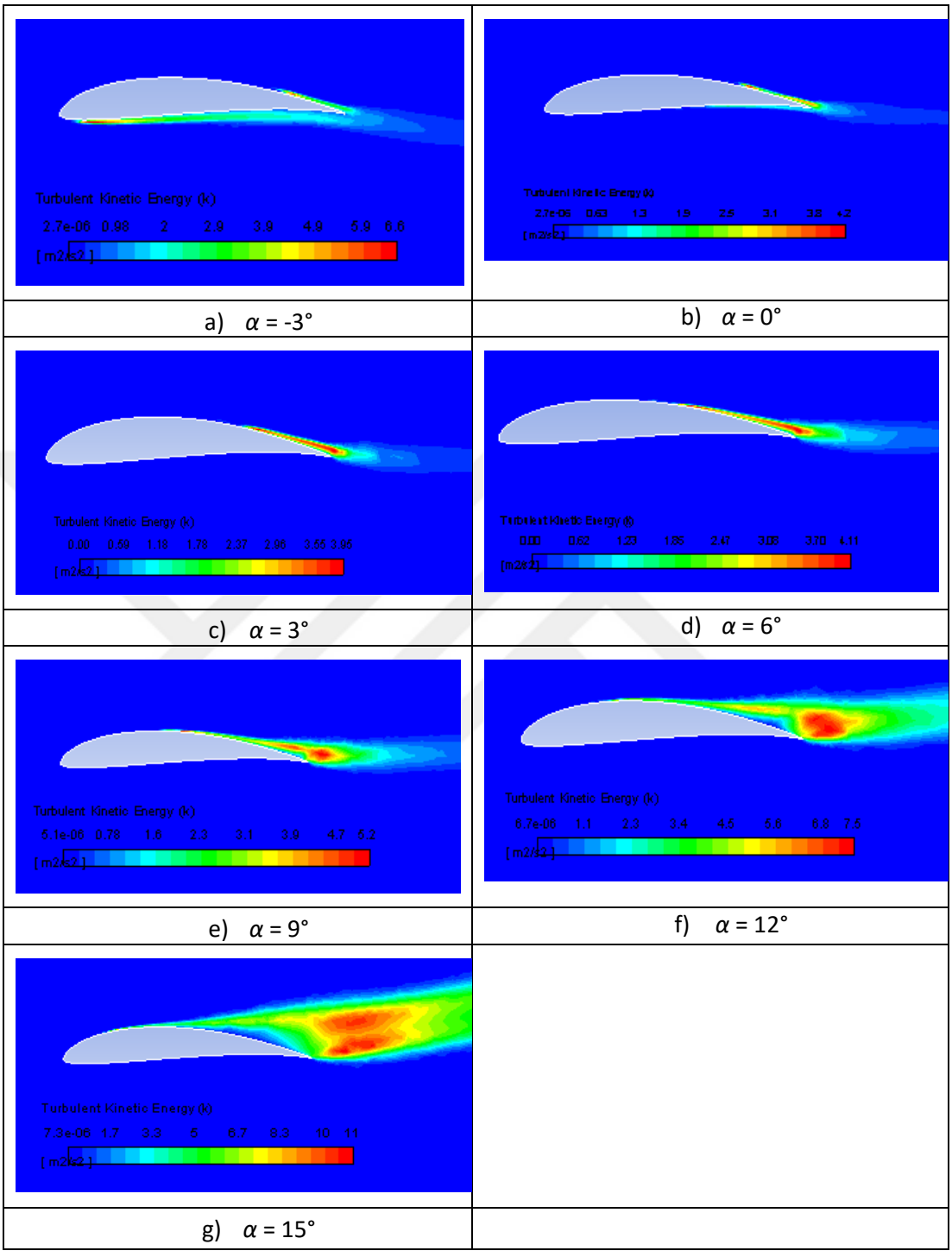


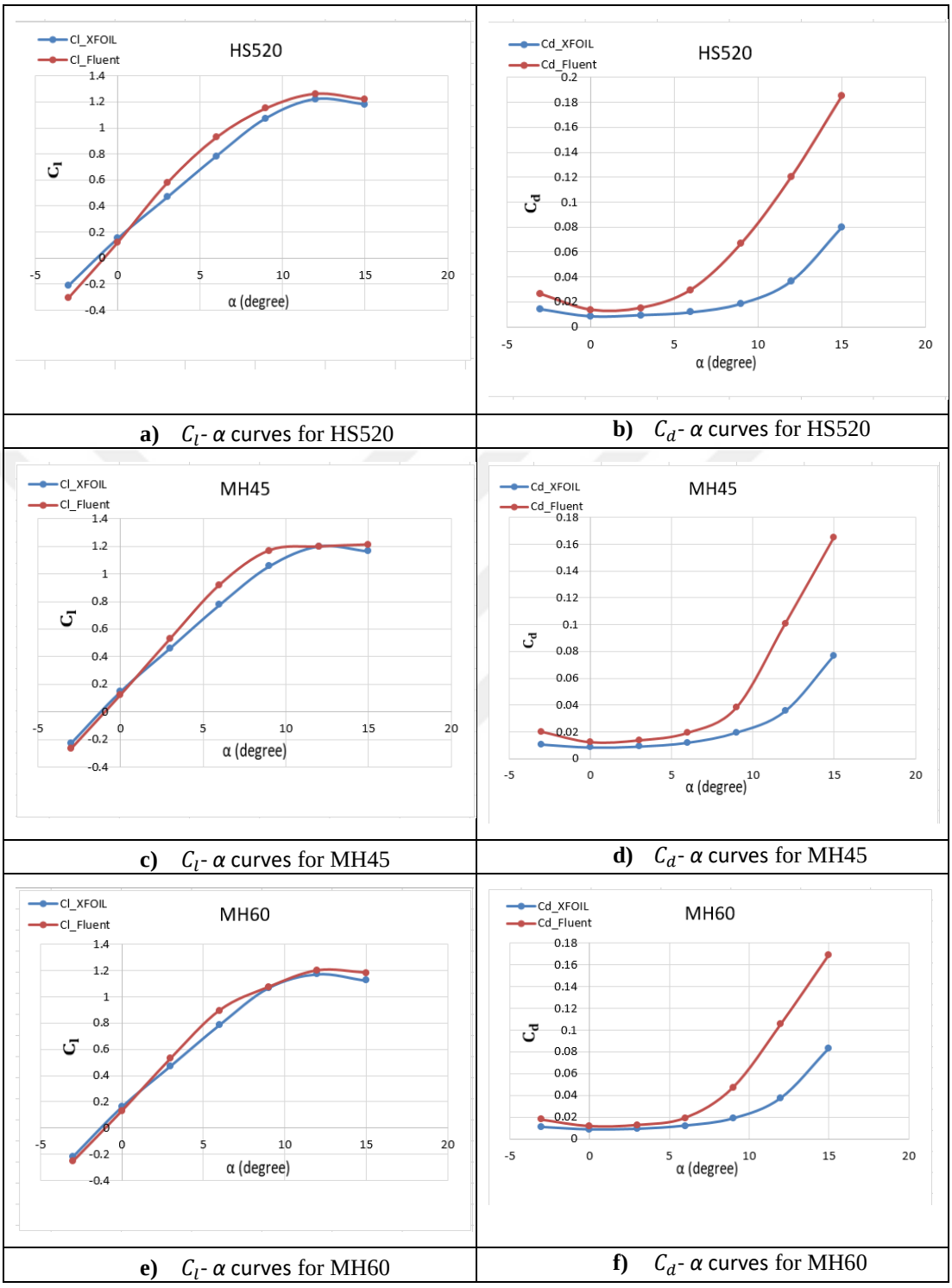
Figure 4.10 Contour of turbulent kinetic energy for different α (-3°, 0°, 3°, 6°, 9°, 12°, 15°) degrees

4.6 Comparison of Fluent and XFOIL Results

Numerical simulations have been performed for all the seven airfoils in XFOIL by loading the coordinate of the airfoils to XFOIL and setting Re number to $2.4 \cdot 10^5$ and Mach number to 0.038 and defining 100 iteration then the graphs of the lift, drag coefficient versus angle of attack have been compared with the corresponding results from Fluent.

Figure 4.11 shows a good correlation between the lift curves of the all airfoils which predicted from Fluent and the corresponding ones predicted from XFOIL. For the drag coefficient prediction in the all airfoils, the shape of the curves corresponds well with XFOILs' and the results are in very good agreement up to angle of attack =9 degree, then the drag graphs of all airfoils in Fluent have increased exponentially. The difference is because of two reasons: the first one is the inaccuracies around stall conditions which are attributable to bad turbulence modeling. The other reason is that due to computational power limitations the structured mesh hasn't been applied in the study, but a hybrid mesh has been applied and in such grid there were some cells had a very small orthogonal quality value which is unwanted property affected negatively on the simulation and caused the undesirable increment in the drag coefficients by increasing the angle of attack.

In general, each one of the programs is using different forms of the governing equations to analyze the flow around airfoils. While FLUENT solves the RANS equations using finite volume discretization, XFOIL code combines a potential flow panel method and an integral boundary layer formulation to deal with such problems which are in both Fluent and XFOIL based on different assumptions and that is what causes the variation in the results.



a) C_l- α curves for HS520

b) C_d- α curves for HS520

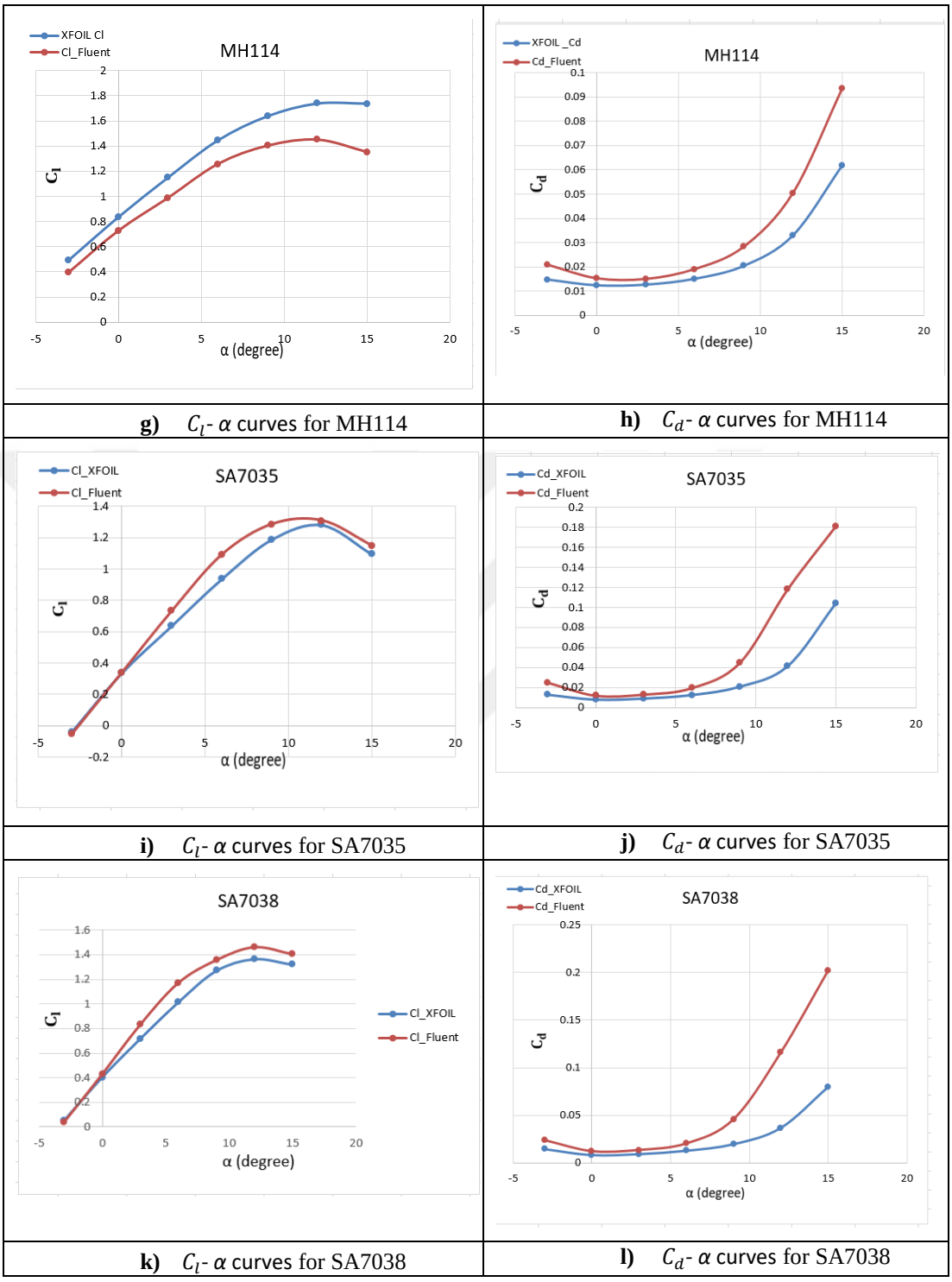
c) C_l- α curves for MH45

d) C_d- α curves for MH45

e) C_l- α curves for MH60

f) C_d- α curves for MH60

Figure 4.11 Lift and drag coefficient graphs for XFOIL and Fluent for the airfoils HS520, MH114, MH45, MH60, SA7035, SA7038, and SD7090 at α (-3°, 0°, 3°, 6°, 9°, 12°, 15°) degrees



g) C_l- α curves for MH114

h) C_d- α curves for MH114

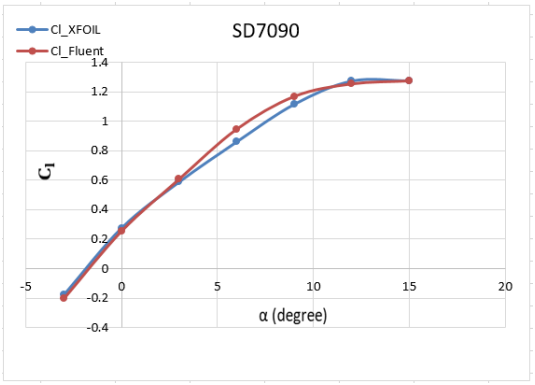
i) C_l- α curves for SA7035

j) C_d- α curves for SA7035

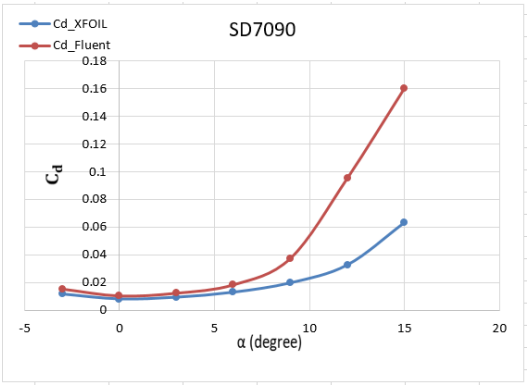
k) C_l- α curves for SA7038

l) C_d- α curves for SA7038

Figure 4.11 (continued) Lift and drag coefficient graphs for XFOIL and Fluent for the airfoils HS520, MH114, MH45, MH60, SA7035, SA7038, and SD7090 at α (-3°, 0°, 3°, 6°, 9°, 12°, 15°) degrees



m) C_l- α curves for SD7090



n) C_d- α curves for SD7038

Figure 4.11 (continued) Lift and drag coefficient graphs for XFOIL and Fluent for the airfoils HS520, MH114, MH45, MH60, SA7035, SA7038, and SD7090 at α (-3°, 0°, 3°, 6°, 9°, 12°, 15°) degrees

CHAPTER 5

CONCLUSIONS

In this study aerodynamic simulations of a group of airfoils were carried out in order to select an optimum airfoil section for small unmanned aerial vehicle designed for surveillance applications taken in account four different criteria through the selection process which were the stalling characteristics of airfoil lift curve, lift to drag ratio, stalling speed and lift coefficient.

Seven different airfoils have been chosen for the comparison study. For each airfoil by using Fluent commercial software, two-dimensional transient case simulation was performed at chord Reynolds number Re= $2.4 \cdot 10^5$ and low subsonic flow speed using Transition Shear Stress Transport (γ-Reθ) SST turbulence model at angle of attack range from -3° to 15° with 3° intervals.

Weighted Scoring selection method have been used for the multi criteria comparing process and end of it Mh114 airfoil section got the maximum weighted score and has been chosen as the best choice among the analyzed airfoils for the designed UAV9. The lift and drag coefficient of the all airfoils which have been predicted from Fluent, have been compared to the corresponding ones predicted from XFOIL and showed a good agreement in C_l values while there were some differences in the results in C_d values at $\alpha > 9°$ in most of the airfoils.

To understand the flow physics of the optimum airfoil better some properties like pressure, velocity and the transition phenomena have been examined in detail.

The examined results showed that with increasing the angle of attack the transition happened closer to the leading edge of the airfoil. The velocity in the upper surface was bigger than its value in the lower surface of the airfoil thus the static pressure was lower in the upper surface than the bottom surface. The low pressure on the upper airfoil surface was greater than the high pressure on the bottom airfoil surface which agrees the principles of aerodynamic. By increasing the angle of attack the airfoil

practiced flow separation because the generating of eddies in the upper surface at the trailing edge.

As a conclusion the MH114 airfoil has fairly satisfied the design requirements and selected to be used as a wing airfoil section in the designed small unmanned aerial vehicle.

REFERENCES

[1] Cai, G., Dias, J., Seneviratne, L. Survey of small-scale unmanned aerial vehicles: Recent advances and future development trends. Unmanned Systems World Scientific Publishing Company, 2, 1-15. 2014.

[2] Beard, R W., Mclain, T W. Small Unmanned Aircraft Theory and Practice. Princeton University Press. 2012.

[3] Barton, J D. Fundamentals of small unmanned aircraft flight. Johns Hopkins APL Technical Digest, 31, 132-149. 2012.

[4] Anderson, J D., Fundamentals of Aerodynamics. 5th Edition. New York: McGraw-Hill companies. 2011.

[5] Anderson, J D., Introduction to Flight. 3rd Edition. New York: McGraw-Hill companies. 1989.

[6] Raymer, D P., Aircraft Design: A Conceptual Approach. 2nd Edition. United States of America: American Institute of Aeronautics and Astronautics, Inc.1992.

[7] Srinath, D N., Mittal, S. Optimal aerodynamic design of airfoils in unsteady viscous flows. Computer Methods in Applied Mechanics and Engineering, 199, 1976-1991. 2010.

[8] Dongli, M., Yanping, Z., Yuhang, Q., Guanxiong, L. Effects of relative thickness on aerodynamic characteristics of airfoil at a low Reynolds number. Chinese Journal of Aeronautics, 28, 1003–1015. 2015.

[9] Kontogiannis, S G., Ekaterinaris, J A. Design, performance evaluation and optimization of a UAV. Aerospace Science and Technology, 29, 339–350. 2013.

[10] Airfoil Tools. Retrieved January 15, 2018, from http://airfoiltools.com

[11] Kovanis, A P., Skaperdas, V., Ekaterinaris, J A. Design and analysis of a light cargo UAV prototype. 4th ANSA & μETA International Conference. 2011.

[12] Hieu, N K., Vinh, P Q., Bao, D A., J A. Design of a Small UAV Combined Between Flying-Wing and Quadrotor with XFRL5. International Journal of Transportation Engineering and Technology, 2, 1-6. 2016.

[13] Aerodesign, Airfoil Database. Retrieved January 10, 2018, from https://www.aerodesign.de/english/profile/profile_s.htm

[14] Yayli, U C., Kimet, C., Duru, A., Cetir, O., Torun, U., Aydogan, A C., Padmanaban, S., Ertas, A H. Design optimization of a fixed wing aircraft. Advances in Aircraft and Spacecraft Science, 4, 65-80. 2017.

[15] Kermode, A C. Mechanics of Flight. 11th Edition. London: Pearson Prentice Hall. 2006.

[16] Choudhry, A., Arjomandi, M., Kelso. K. A study of long separation bubble on thick airfoils and its consequent effects. International Journal of Heat and Fluid Flow, 52, 84-96. 2015.

[17] Genc, M. S., Karasu, I., Acıkel, H. H., An experimental study on aerodynamics of NACA2415 aerofoil at low Re numbers. Experimental Thermal and Fluid Science, (39), 252-264. 2012.

[18] Selig, Donovan, and Fraser. Airfoils at Low Speeds. USA.: H. A. Stokely. 1989.

[19] Koca, K., Genç, H H., Çağdaş, M., Bodur. T M. Identification of flow phenomena over NACA 4412 wind turbine airfoil at low Reynolds numbers and role of laminar separation bubble on flow evolution. Energy, 144, 750-764. 2018.

[20] Castiglioni, G., Domaradzki, J. A., Pasquariello, V., Hickel, S., Grilli, M. Numerical simulations of separated flows at moderate Reynolds numbers appropriate for turbine blades and unmanned aero vehicles. International Journal of Heat and Fluid Flow, 49, 91-99. 2014.

[21] CFD Online, Y plus wall distance estimation. Retrieved April 12, 2018, from https://www.cfdonline.com

[22] ANSYS Meshing User's Guide. Release 17.0. U.S.A. ANSYS, Inc. 2016.

[23] Introduction to ANSYS Meshing: Lecture 8 Mesh Quality Release 14.5.

[24] ANSYS FLUENT User's Guide Release 14.0. U.S.A. ANSYS, Inc. 2011.

[25] Aftab, S M A., Rafie, A S M., Razak, N A., Ahmad, K A. Turbulence Model Selection for Low Reynolds Number Flows. PLOS ONE. 2016.

[26] Lanfrit, M. Best practice guidelines for handling Automotive External Aerodynamics with FLUENT. 2005.

[27] Turbulence Modeling Using ANSYS Fluent: Lecture 2 Near-Wall Modeling and Transition Modeling. Release 15.0.

[28] Engineering Tool Box, International Standard Atmosphere. Retrieved April 7, 2018, from https://www.engineeringtoolbox.com/international-standard-atmosphere-d_985.html 2005

[29] Introduction to ANSYS Fluent**:** Lecture 3 Cell Zone and Boundary Conditions**.** Release 16.0.

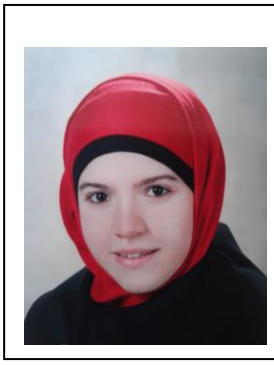
[30] Keating, M. Accelerating CFD Solutions. ANSYS Advantage, V, 2011.

[31] ANSYS Fluent Tutorial Guide Release 16.0 ANSYS, Inc. 2015.

[32] Introduction to ANSYS Fluent: Lecture 10 Transient Flow Modeling. Release 16.0.

[33] Sadraey, M H., Aircraft Design a Systems of Engineering Approach. India: Wiley. 2013.

CURRICULUM VITAE



PERSONAL INFORMATION

Name Surname : Raghad BABA

Date of Birth : 07.05.1990

Phone : +90 505 140 62 31

E-mail : baba.raghad@gmail.com

EDUCATION

High School : Nablus High School - Aleppo/Syria (2005-2008)

Bachelor : Aleppo University - Aleppo/ Syria (2008-2013)

Master's Degree : Ankara Yildirim Beyazit University/Ankara/Turkey (2015-continued)

WORK EXPERIENCE

Arabic -Turkish Interpreter : United Nations High Commissioner for Refugees - UNHCR (15.11.2018 - continued)

Intern : İş Sağlığı ve Güvenliği Araştırma ve Geliştirme Enstitüsü Başkanlığı İSGÜM (02.07.2018 17.08.2018)